ISSN : 2830-8085

Journal of Physical & Chemical Research

Volume **1** June (2022) 1-71

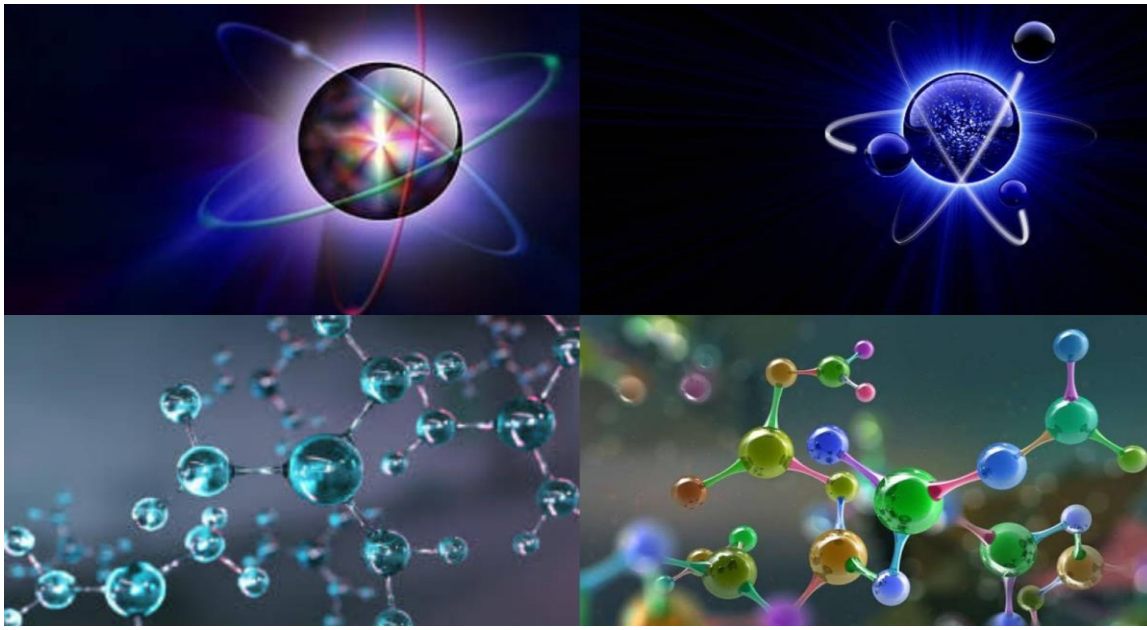

Pr. Kahoul Abdelhalim
Editor-in-Chief

Journal homepage: https://www.univ-bba.dz

Journal of Physical and Chemical Research

- **Scientific committee**

- Laraoui Abdelghani
  alaraoui2@unl.edu
  Department of Mechanical & Materials Engineering, University of Nebraska – Lincoln, USA.
- Nuray Kup Aylikci
  nuray.aylikci@iste.edu.tr
  Department of Energy Systems Engineering, Faculty of Engineering and Natural Sciences.
  Iskenderun Technical University, Iskenderun, Hatay, Turkey.
- Volkan Aylikci
  volkan.aylikci@iste.edu.tr
  Department of Metallurgical and Materials Engineering,
  Faculty of Engineering and Natural Sciences, Iskenderun Technical University,
  Iskenderun, Hatay, Turkey.
- Sarra Mustapha
  sarramust1@yahoo.fr
  Mohamed El Bachir El Ibrahimi University, Bordj-Bou-Arreridj, Algeria.
- Latrache Abdelhakim
  abdelhakim.latreche@univ-bba.dz
  Mohamed El Bachir El Ibrahimi University, Bordj-Bou-Arreridj, Algeria.
- Abdelhalim Bencheikh
  abdelhalim.bencheikh@univ-bba.dz
  Mohamed El Bachir El Ibrahimi University, Bordj-Bou-Arreridj, Algeria.
- Bentabet Abdelouahab
  abdelouahab.bentabet@univ-bba.dz
  Mohamed El Bachir El Ibrahimi University, Bordj-Bou-Arreridj, Algeria
- Lebgaa Nodjoud
  noudjoud.lebga@univ-bba.dz
  Mohamed El Bachir El Ibrahimi University, Bordj-Bou-Arreridj, Algeria.
- Bahloul Ahmed
  ahmed.bahloul@univ-bba.dz
  Mohamed El Bachir El Ibrahimi University, Bordj-Bou-Arreridj, Algeria.
- Hellati Abdelhak
  abdelhak.hellati@univ-bba.dz
  Mohamed El Bachir El Ibrahimi University, Bordj-Bou-Arreridj, Algeria.
- Boufassa Samia
  samia.boufassa@univ-bba.dz
  Mohamed El Bachir El Ibrahimi University, Bordj-Bou-Arreridj, Algeria.
- Benamrani Ammar
  ammar.benamrani@univ-bba.dz
  Mohamed El Bachir El Ibrahimi University, Bordj-Bou-Arreridj, Algeria.
- Daoud Salah
  salah.daoud@univ-bba.dz
  Mohamed El Bachir El Ibrahimi University, Bordj-Bou-Arreridj, Algeria.
- Riad Ayache
  riad.ayache@univ-bba.dz
  Mohamed El Bachir El Ibrahimi University, Bordj-Bou-Arreridj, Algeria.
- Khelladi Mohamed Ridha
  mohamedridha.khelladi@univ-bba.dz ; redha2022@yahoo.fr
  Mohamed El Bachir El Ibrahimi University, Bordj-Bou-Arreridj, Algeria.
- Tabti Salima
  salima.tabti@univ-bba.dz ; thabti_sa@yahoo.fr
  Mohamed El Bachir El Ibrahimi University, Bordj-Bou-Arreridj, Algeria.

- Chikouche Imene
  imene.chikouche@univ-bba.dz ; chikouche_imene@yahoo.fr
  Mohamed El Bachir El Ibrahimi University, Bordj-Bou-Arreridj, Algeria.
- Khalfallah Farid
  f.khalfallah@univ-bba.dz ; khal.far@gmail.com
  Mohamed El Bachir El Ibrahimi University, Bordj-Bou-Arreridj, Algeria.
- Daoudi Salim
  s.daoudi@univ-bba.dz ; salzdg@gmail.com
  Mohamed El Bachir El Ibrahimi University, Bordj-Bou-Arreridj, Algeria.
- Sahnoune Yassine
  yassine.sahnoune@univ-bba.dz ; sahnoun.y34@gmail.com
  Mohamed El Bachir El Ibrahimi University, Bordj-Bou-Arreridj, Algeria.
- Bioud Nadhira
  nadhira.bioud@univ-bba.dz
  Mohamed El Bachir El Ibrahimi University, Bordj-Bou-Arreridj, Algeria
- Kasri Yazid
  yazidkasri@yahoo.fr
  University of Béjaia.
- Deghfel Bahri
  badeghfel@gmail.com
  University of M'sila
- Baadji Nadjib
  nadjibbaadji@gmail.com
  University of M'sila
- Lamiri Leila
  l.lamiri@crti.dz
  Unité de Développement des Couches, Minces et Applications (UDCMA-CRTI), Sétif.
- Laidoudi Samiha
  s.laidoudi@crti.dz
  Unité de Développement des Couches, Minces et Applications (UDCMA-CRTI), Sétif.
- Belgherbi Ouafia
  o.belgherbi@crti.dz
  Unité de Développement des Couches, Minces et Applications (UDCMA-CRTI), Sétif.
- Kaabi Ilhem
  Kaabi.ilhem@univ-setif.dz
  Ferhat Abbas University -Sétif 1-, Algeria.
- Boudour Samah
  s.boudour@crti.dz
  Unité de Développement des Couches Minces et Applications (UDCMA-CRTI)
- Belhadj Hamza
  email: hbelhadj@cdta.dz , belhadjhamza@gmail.com
  Unité de Recherche en Nanosciences et Nanotechnologies
  Centre de Développement des Technologies Avancées (CDTA)
- Hamza Djamel
  Email : djamel.hamza@univ-setif.dz
  Département de chimie, Faculté des Sciences, Université Ferhat ABBAS- Sétif 1
- Hayette Faid
  hayettefaid@univ-bba.dz
  Mohamed El Bachir El Ibrahimi University, Bordj-Bou-Arreridj, Algeria.
- Fares Nor El Houda
  norelhouda.fares@univ-bba.dz; fares_houda@yahoo.fr
  Département Recherche Opérationnelle, Faculté Mathématiques et Informatiques
  Mohamed El Bachir El Ibrahimi University, Bordj-Bou-Arreridj, Algeria

Journal of Physical and Chemical Research
Volume 1 June (2022) 1-71

Physical Research

Chemical Research

Journal of Physical & Chemical Research

Journal homepage:

Structural properties of $NaBeH_3$ material: *Ab-initio* calculations

Merriem Rahrah[1,2*], Noudjoud Lebga[2,3], Abdelhakim Latreche[1,2], Salah Daoud[4]

[1]Laboratory of Materials Physics, Radiation and Nanostructures (LPMRN), Mohamed El Bachir El Ibrahimi University, 34000 Bordj Bou-Arreridj, Algeria
[2]Department of Matter Science, Faculty of Sciences and Technology, Mohamed El Bachir El Ibrahimi University, 34000, Bordj Bou-Arreridj, Algeria
[3]Optoelectronic and Compounds Laboratory, Department of Physics, Ferhat Abbas University of Setif 1, 19000 Setif, Algeria
[4]Laboratory of Materials and Electronic Systems, Faculty of Sciences and Technology, Mohamed El Bachir El Ibrahimi University of Bordj Bou Arreridj, 34000 Bordj Bou Arreridj, Algeria.
** Corresponding author: Tel./Fax: +0-000-000-0000 ; E-mail address: noudjoud.lebga@univ-bba.dz*

Article history
Received March 16, 2022
Accepted for publication March 21, 2022

Abstract

Ab-initio calculations from first principle methods were performed to investigate the structural properties of perovskite-type hydride $NaBeH_3$ material. The pseudopotential plane-wave approach in the framework of density functional theory (DFT) as implemented in the ABINIT code computer was used. The exchange-correlation functional for all elements of our material of interest was described with the local density approximation (LDA). Our results of the equilibrium lattice parameter, the bulk modulus, and the pressure derivative of the bulk modulus of cubic $NaBeH_3$ semiconducting material were found at around 3.335 Å (3.339 Å), 65.64 GPa and 3.56, respectively. Our data are in good agreement with the available theoretical data of the literature. In addition, the melting point of our material of interest was calculated and found equal to 1217.45 K. To the best of the authors' knowledge, no data is available in the literature on the melting point of $NaBeH_3$ material.

Keywords: Ab-initio calculations, DFT, local density approximation (LDA), structural properties, perovskite-type hydride.

1. Introduction

Hydrogen is the fuel of the future, which is stored in many ways as a compressed gas, as liquid in suitable containers, or sometimes as solid in metal and complex hydrides [1-3]. Among the most important factors that determine the ability of materials to store hydrogen is the crystal structure and its shape and surface composition [3-5]. One of the complex hydrides used in hydrogen storage is $NaBeH_3$. Many theoretical studies on perovskite-type hydride $NaBeH_3$ semiconducting material have been carried out using *ab initio* calculations with many approaches [6-8]. In this study, we focus on cubic perovskite-type $NaBeH_3$ semiconductor and discuss the method used in the calculation as well as the results obtained from structural properties.

2. Method of calculations

The first-principle calculations were performed by employing pseudopotential plane-waves (PP-PW) approach based on the density functional theory (DFT) [9] as implemented in the ABINIT code [10]. ABINIT code computer is a common project of the Université Catholique de Louvain, Corning Incorporated, and other contributors. We used the Teter and Pade parameterization [11] for the local density approximation (LDA). Only the outermost electrons of each atom were explicitly considered in the calculation. The effect of the inner electrons and the nucleus was described within a pseudopotential scheme. We used the Trouiller-Martins scheme [12] to generate the norm-conserving nonlocal pseudopotentials, which results in highly transferable and optimally smooth pseudopotentials. A plane-wave basis set was used to solve the Kohn-Sham equations in the pseudopotential implementation of the DFT-LDA. The Brillouin zone integrations were replaced by discrete summations over a special set of *k*-points, using the standard *k*-point technique of Monkhorst and Pack [13] where the *k*-point mesh used is (6 × 6 × 6). The plane wave energy cut-off to expand the wave functions is set to be 60 Hartree.

3. Results and discussions

The structure discussed in this work is cubic perovskite-type $NaBeH_3$ (space group Pm3m) [5, 8] with a unit cell of 5 atoms (one atom of Na, one atom of Be, and three atoms of H). They are positioned in the following positions: Be (0, 0, 0), Na (1/2, 1/2, 1/2) and H (0, 0, 1/2), respectively. The structure of cubic perovskite-type $NaBeH_3$ is shown in Figure 1.

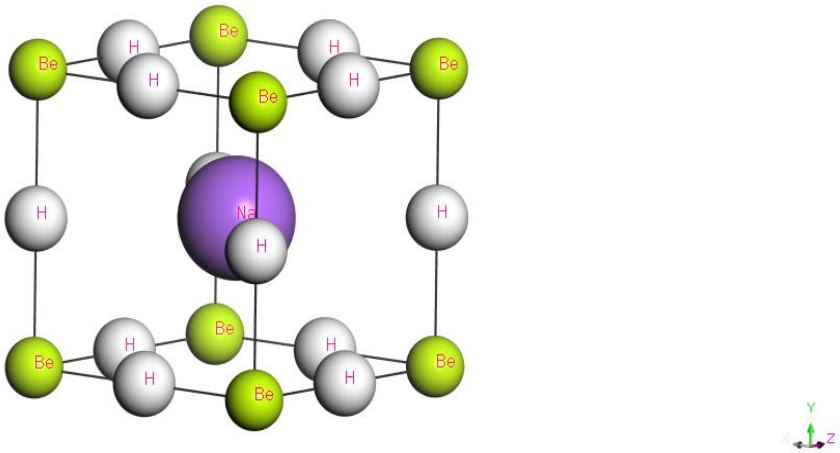

Figure 1. Crystal structure of cubic $NaBeH_3$ perovskite-type hydride material.

Usually, before starting simulations of different physical properties for a studied material using the Abinit code computer, it is necessary to know the optimal values of two important quantities, i.e., the plane wave kinetic energy cutoff (E_{cut}) and the grid of special *k*-points (nkpt) [14-16]. The kinetic energy cutoff and the number *k*-points are two parameters which can have an enormous effect on the quality of the calculation [17]. These two parameters are not known in advance when launching a calculation. Increasing the values of E_{cut} and nkpt considerably affects the value of the total energy, as shown in Figure. 2 (a) and (b).

To expand the wave functions, we used a value of 60 Ha (1 Hartree = 27.211396 eV) for E_{cut}, and the Brillouin zone integrations were replaced by discrete summations over a special set of k-points using the standard *k*-point technique of Monkhorst and Pack with 6 x 6 x 6 meshes. Using the verified values of cutoff energy and k-point mesh, the relative energy converged to better than 10^{-5} Hartree.

After having determined the kinetic energy cut-off and the number of special *k*-points which gives the best convergence possible of total energy, they are used to calculate total energy for various values of the lattice constant. Energies were calculated for various values of the lattice constant, the different values obtained are then presented as function of the unit cell volume.

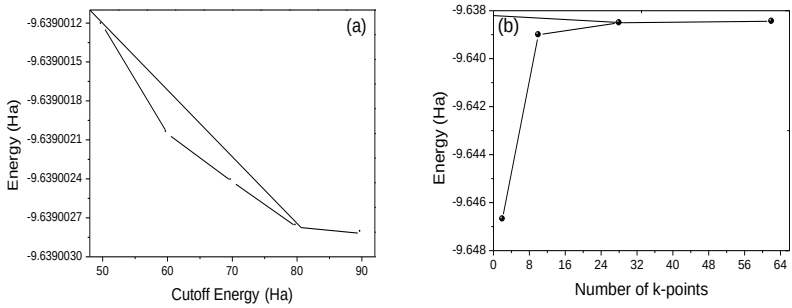

Figure 2. Total energy of cubic structure $NaBeH_3$ as a function of E_{cut} off (a) and k-points (b).

From the total energy E_{Tot} presented as a function of the lattice volume V, one can deduce the static structural properties such as the equilibrium lattice constant from the volume which gives the minimum energy, the bulk modulus B_0 and its pressure derivatives B_0' by fitting the total energy with so-called Birch Murnaghan's equation which have the following expression: [18, 19]

$$E_{total}(V) - E_0(V) = \frac{B_0 V}{B'(B'-1)}\left[B\left(1-\frac{V_0}{V}\right) + \left(\frac{V_0}{V}\right)^{B'} - 1\right] \quad (1)$$

where, V_0 is the equilibrium unit-cell volume, while $E(V_0)$ is the corresponding energy.

Figure 3 shows the evolution of the total energy as a function of the unit cell volume of cubic perovskite-type $NaBeH_3$. The equilibrium lattice parameter was computed also from the structural optimization, using the Broyden-Fletcher-Goldfarb-Shanno (BFGS) [20] minimization.

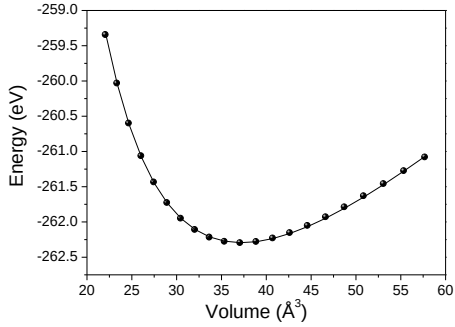

Figure 3. Total energy per formula unit of cubic $NaBeH_3$ versus volume.

The results of the lattice parameter a_0 obtained from the fit of the Birch Murnaghan equation and from the BFGS technique, that of bulk modulus B_0, and that of its pressure derivative B'_0 are reported in Table 1, and compared with the available theoretical data [6, 7, 8, 21]. The calculated lattice parameters, bulk modulus and its pressure derivative of cubic $NaBeH_3$ are in good agreement with the previous studies.

Table 1. Optimized equilibrium structural parameters a (Å) (^{a} from the relation of Eq. (1), ^{b} from the BFGS technique), bulk modulus B_0 (GPa), and pressure derivative of bulk modulus (B'_0) for cubic $NaBeH_3$.

	Our data LDA	**Other calculus**			
		LSDA	**GGA**	**WC-GGA**	**PBE-GGA**
a (Å)	3.335^a, 3.339^b	3.281 [8]	3.318 [7], 3.2662 [21]	3.350 [8]	3.352 [6], 3.352 [7]
B_0 (GPa)	65.64 ^{a}	65.92 [8]	62.7 [7], 62.7 [21]	61.06 [8]	61.55 [7]
B'_0	3.56 ^{a}		3.5 [21]		

For several materials having a cubic structure, the melting point T_m correlates with the bulk modulus B by an linear empirical formula, which is expresses as follow [22, 23]:

$$T_m = 9.3B + 607 \quad (2)$$

where the melting point T_m is expressed in K, while the bulk modulus B is expressed in GPa.

Using the previous expression, the melting point T_m of $NaBeH_3$ material was found equal to 1217.45 K. This value is very lower than the values 2264.30± 30 K and 1758.05 ± 300 K of T_m reported for BAs and BSb semiconducting material, respectively [24]. Unfortunately, to the best of the authors' knowledge, the melting point T_m of cubic $NaBeH_3$ material has never been previously reported in the literature.

4. Conclusion

In this study, the equilibrium lattice constant, the bulk modulus, and the pressure derivative of bulk modulus of the cubic $NaBeH_3$ material were determined using the pseudopotential plane-wave method within the local density approximation (LDA). Our calculated ground state parameters agree well with the other available results of the literature. The melting point of $NaBeH_3$ material was also predicted, and found at around 1217.45 K. To the best of our knowledge; there is no other theoretical data or experimental values of T_m for $NaBeH_3$ material to make comparison.

References

[1] B. Bogdanović, M. Schwickardi. J. Alloys Compd. **253** (1997) 1-9.
[2] C. M. Jensen, K. Gross. Appl. Phys. A. **72** (2001) 213-219.
[3] H. Morioka, K. Kakizaki, S.C. Chung, A. Yamada. J. Alloys Compd. **353** (2003) 310-314.
[4] J. Block, A. P. Gray. Inorg. Chem. **4** (1965) 304-305.
[5] P. Vajeeston, P. Ravindran, H. Fjellvåg. Inorg. Chem. **47** (2008) 508-514.
[6] A. H. Reshak. J. Catal. **351** (2017) 119-129.
[7] S. Xiao-Jiao, H. Zhi, M. Yan-Ming, C. Tian, L. Bing-Bing, Z. Guang-Tian. Chin. Phys. B. **17** (2008) 2222-2228.
[8] B. Rehmat, M. A. Rafiq, Y. Javed, Z. Irshad, N. Ahmed, S. M. Mirza. Int. J. Hydrogen Energy. **42** (2017) 10038-10046.
[9] W. Kohn, L. Sham. J. Phys. Rev. A **140** (1965) 1133-1138.
[10] The ABINIT computer code is a common project of the Universite Catholique de Louvain, Corning Incorporated, and other contributors. (URL http: //www.abinit.org)
[11] S. Goedecker, M. Teter, J. Hutter. Phys. Rev. B **54** (1996) 1703-1710.
[12] N. Troullier, J.L. Martins. Phys. Rev. B **43** (1991) 1993-2006.
[13] H. J. Monkhorst, J. D. Pack. Phys. Rev. B **13** (1976) 5188-5192.
[14] N. Lebga, Propriétés structurales, élastiques et optiques de semiconducteurs à grand gap: Les composés BV, les alliages $Zn_xCd_{1-x}Se$ et $ZnSe_{1-x}Te_x$, le β-SiC, Doctoral dissertation, Ferhat Abbas University, Setif, Algeria (2011).
[15] S. Daoud, N. Bioud, N. Lebgaa, R. Mezouar. Int. J. Phys. Res. **2** (2014) 27-31.
[16] S. Daoud, N. Bioud. Int. J. Phys. Res., **2** (2014) 50-55.
[17] S. Daoud, N. Bouarissa. Theor. Chem. Accounts. **138** (2019) 49-.
[18] F. D. Murnaghan. Proc. Natl. Acad. Sci. U. S. A. **30** (1944) 244-247.
[19] S. Daoud, N. Bioud, N. Lebga. J. Optoelectron. Adv. Mater. **16** (2014) 207-214.
[20] C.G. Broyden. J. Inst. Math. Appl. **6** (1970) 222-231.
[21] P. Vajeeston, P. Ravindran, H. Fjellvåg. J. Alloys Compd. **446-447** (2007) 44-47.
[22] M.E. Fine, L.D. Brown, H.L. Marcus. Scr. Mater. **18** (1984**)** 951-956.
[23] T. Özer. Can. J. Phys. **98** (2020) 357-363.
[24] S. Daoud. Int. J. Sci. World. **3** (2015) 43-48.

Journal of Physical & Chemical Research

Journal homepage:

Analysis of the quasi exact solvable Rydberg dressed atoms interaction model

Nabila Grar[1,*], Leila Chia[1,2]

[1]*Department of Matter Sciences, Faculty of Sciences and Technology, Mohamed El Bachir El Ibrahimi University, Bordj-Bou-Arreridj 34030, Algeria.*
[2]*Laboratory of Materials Physics, Radiation and Nanostructures (LPMRN), Faculty of Sciences and Technology, Mohamed El Bachir El Ibrahimi University, Bordj-Bou-Arreridj 34030, Algeria.*

** Corresponding author: E-mail address: nabila.grar@univ-bba.dz*

Article history
Received March 20, 2022
Accepted for publication March 31, 2022

Abstract

The exact solvable model of the Rydberg dressed interaction for two particles proposed by Kościk et al. is analyzed in the different dimensions to single out the impact of the dimensionality. First we analyze the effect on the energy spectrum then spatial correlations are studied as the radial density distribution versus the position in the three dimensionalities. The results clarify the effect of the centrifugal forces in the presence of long range interaction.

Keywords: long range interaction, cold atoms, confined atoms, quasi solvable models.

1. Introduction

Experiments involving confined cold few particles are nowadays a matter of routine. In fact number of systems parameters as the confinement potential and the particle-particule interaction features can be controlled on demand [1] [2]. This way, it is possible to verify experimentally the validity of a number of quantum simplified models studied by the past. It is however also true that more efforts are necessary in order to devise new “toy” models aiming at a detailed comprehension of the features of the interaction at different level of approximation as well as different dimensionalities.

Exact solution for the Schrodinger equation established for the case of different and sometimes complicated potentials can be found in the literature (see for example [3]). Most of these solutions are given for the case of single particle systems. The situation becomes quite complicated

when considering the case of two particles as a first step on the path towards cold confined mesoscopic systems. The difficulty resides in the consideration of both confinement potential characteristics as well as realistic interaction between particles. The hard core interaction is the most simplified scheme of interaction and in this case it is possible to achieve exact solution for two particles systems by implementing the Bethe ansatz[4]. A theoretical work encompassing the three dimensionalities and a delta like interaction for a system of two particles was elaborated by Bush et al.[5]. A quasi exact solution is hence established where the interaction could be considered to be of contact nature (an s-wave for bosons and p-wave for fermions). This interaction model however ignores the long range nature of interaction for dipolar atoms or Rydberg dressed interaction behaving as $1/r^6$[6]. An analytical solution for this interaction is still to be elaborated. Nevertheless a simplification of this interaction as a step function was proposed by Kościk et al[7]. It was possible in this case to reach a quasi exact solution in one and two dimensions and a study of the different features of the system was elaborated. This kind of quasi solvable models are of extreme importance for advances in cold confined few particles systems. It can be considered as a set of models to be validated experimentally as well as an exact basis to construct the solution for few body systems exploiting different strategies (as variational, ab initio, interacting configurations..) The aim of our present study is to elaborate a comparative analysis of the quasi exact solvable model of Kościk et al. in the three dimensionalities and highlight the most important players for the considered interaction.

2. Theoretical approach

The aim of the different models is to establish an analytical solution for the following Schrodinger equation for a system of two particles having the same mass m:

$$\sum_{i=1}^{2}\frac{-\hbar^2}{2m}\nabla_i^2+\left(V_{ext}+v_{inter}\right)\psi\left(\vec{r}_1,\vec{r}_2\right)=E\psi\left(\vec{r}_1,\vec{r}_2\right) \qquad (1)$$

Where V_{ext} is the confining potential, v_{inter} is the interaction potential depending on the particles separation and r_i is the vector position for each particle. The confining potential is considered to be harmonic and the dimensions considered in the harmonic oscillator will define the constraint on the motion of the particles and consequently will define the dimensionality of the problem. The same confining potential is imposed to both particles and the equation becomes:

$$\left(\sum_{i=1}^{2}\left(\frac{-\hbar^2}{2m}\nabla_i^2+\frac{1}{2}m\omega^2 r_i^2\right)+v_{inter}\left(\left|r_1-r_2\right|\right)\right)\psi\left(\vec{r}_1,\vec{r}_2\right)=E\psi\left(\vec{r}_1,\vec{r}_2\right) \qquad (2)$$

For this quadratic potential it is possible to single out the center of mass

contribution to the motion from the radial one and we can write the equation as:

$$\left(\frac{-\hbar^2}{2M}\nabla^2_{\vec{R}}+\frac{1}{2}M\omega^2R^2+\frac{-\hbar^2}{2\mu}\nabla^2_{\vec{r}}+\frac{1}{2}\mu\omega^2r^2+v(r)-E\right)\psi(\vec{R},\vec{r})=0 \quad (3)$$

where $M=2m$, $\mu=m/2$, $\vec{R}=(\vec{r}_1+\vec{r}_2)/2$ and $\vec{r}=\vec{r}_1-\vec{r}_2$

The wave function can be written in a separable form as:

$$\psi(\vec{R},\vec{r})=\varphi(\vec{R})\ \phi(\vec{r}) \quad (4)$$

Consequently we can separate the center of mass and the relative motion equations as:

$$\left(\frac{-\hbar^2}{2M}\nabla^2_{\vec{R}}+\frac{1}{2}M\omega^2R^2-E_c\right)\varphi(\vec{R})=0 \quad (5)$$

and

$$\left(\frac{-\hbar^2}{2\mu}\nabla^2_{\vec{r}}+\frac{1}{2}\mu\omega^2r^2+v(r)-E_r\right)\ \phi(\vec{r})=0 \quad (6)$$

with $E=E_c+E_r$.

The first equation is just an equation for a harmonic oscillator with known solutions and the difficulty resides in finding a solution for the second equation where handling a realistic interaction can be quite challenging.

In one dimension (say for example $x=x_1-x_2$) the relative equation reduces to :

$$\left(\frac{-d^2}{dx^2}+\frac{1}{4}x^2+v(x)-E_r\right)\ \phi(x)=0 \quad (7)$$

Here the equation is written such as the energy and the position are expressed in $\hbar\omega$ and $\sqrt{\frac{\hbar}{m\omega}}$ units respectively.

For two dimensions we convert to polar coordinate $\vec{r}\rightarrow(r,\varphi)$ and with writing the relative wave function as:

$$\phi(r,\varphi)=\frac{1}{\sqrt{r}}\ f(r)e^{\pm i\varphi} \quad (8)$$

The equation for the radial part becomes:

$$\left(\frac{-d^2}{dr^2}+\frac{l^2-1/4}{r^2}+\frac{r^2}{4}+v(r)-E_r\right)f(r)=0 \quad (9)$$

Where l is the angular momentum quantum number and it is expressed in $\sqrt{\hbar m\omega}$ units.

For three dimensions we use spherical coordinates $\vec{r}\rightarrow(r,\theta,\varphi)$ the

relative wave function is written as:

$$\phi(r,\theta,\varphi)=\frac{1}{r}f(r)y_l^m(\theta,\varphi) \tag{10}$$

and the equation for the radial part is then given as :

$$\left(\frac{-d^2}{dr^2}+\frac{l(l+1)}{r^2}+\frac{r^2}{4}+v(r)-E_r\right)f(r)=0 \tag{11}$$

Solving these different equations ((7),(9) and(11)) will rely on the form considered for the interaction potential. As matter of fact different forms of the interaction are studied in the literature starting from the hard core potential or impenetrable hard sphere defined as :

$$\begin{cases} v(r)=\infty \quad for \quad 0\le r\le r_0 \\ \quad v(r)=0 \quad \text{elsewhere} \end{cases} \tag{12}$$

r_0 is the radius of the sphere and the Schrodinger equation is solved by considering that the wave function is exactly zero inside the sphere.

The potential is also considered to be of a contact nature and in this case it is given as delta function as:

$$\begin{cases} v(x)=g\delta(x-x_0) \quad for \qquad 1\,\text{dimension} \\ v(r)=g\dfrac{\partial}{\partial r}r\delta(r-r_0)\ for \qquad 2 \text{ and } 3 \text{ dimensions} \end{cases} \tag{13}$$

Where g is the strength of the interaction.

We notice that the delta function must be regularized in order to avoid singularity in two and three dimensions[5]. Taking this into account it was possible to solve quasi exactly the problem for the three dimensions.

In order to consider the long range nature of the interaction otherwise the dipolar interaction between two non symmetric neutral charged atoms we should consider a short ranged part of the interaction to which we add a van der waal long ranged interaction. In this case the interaction potential can be given as:

$$v(r)=\frac{g}{1+(r/R_c)^6} \tag{14}$$

Where g gives the strength and R_c is the range of the potential respectively.

It is not possible yet to find an exact solution to the equations (7) (9) (11) with this realistic interaction but a quasi exact solution was achieved for a potential defined as a step function that mimics the previous expression quite fairly for the short range part and then falls abruptly to zero otherwise and is given as:

$$\begin{cases} v(r) = V_0 \quad \text{for} \quad 0 \le r \le a \\ v(r) = 0 \quad \text{elsewhere} \end{cases} \tag{15}$$

Where we can relate V_0 and a to the strength and the range (g and R_C) respectively.

In this case it is possible to establish a quasi exact solution by reducing the radial equation to a Weber form in the case of one dimension and a Kummer form for two and three dimensions and the solution is expressed as function of the confluent hypergeometric function of the first kind *1F1* in the region [0,a] and as function of the Tricomi function *U* elsewhere. In order to guarantee a physical behavior of the whole solution a condition for the continuity of the two functions and their derivative is imposed at $x=a$ and henceforth this gives rise to the quantification of the energy which allows to retrieve the energy spectrum with different combination of strength V_0 and the range a[7]. 0

3. Energy spectrum and impact of the dimensionality

In order to study the effect of the interaction strength and its range, we have elaborated programs in C language for the three dimensionalities. The continuity equation is resolved in order to find the eigen energy for different couple(V_0,a). The wave function is then used to calculate the probability density and other related quantities. We follow the prescription given in[7] to extend the results already known for one and two dimension to three dimensions. Let us now show some of the results we can achieve by exploiting the solutions provided by the previous model bearing in mind that the comparison is made relative to V_0=0 where we retrieve the simple equidistant spectrum for a harmonic oscillator. First we can show the effect of the different values of the couple (V_0,a) on the energy spectrum. On figure 1 we are depicting the energy of the fundamental level n=0 with different value of the angular momentum quantum number l=0,1,2,3 and 4. The energy is plotted versus V_0 and the different panels are for different ranges of the interaction. We can see on this figure that levels with increasing value of *l* are affected by the interaction as its range is increased and that the most important impact is observed when the interaction is attractive (V_0 negative). In this case the eigen energy is as negative as the interaction is attractive forcing the system to be in a bound state. When redoing the same figure for n=1 one can see that the energy levels are less affected by the interaction and we have to reach a range as high as 1.25 to obtain a noticeable change for the attractive part of the interaction.

These findings show the effect of the centrifugal force which scales as the square of the angular moment and acts in a way to repel the system at a separation where it does not feel the effect of the interaction. These results are to be contrasted with the case of one dimension in figure 3 where we can see that the absence of an angular momentum makes that

all the curves are more or less equally affected by the attractive interaction depending only on the range of the interaction and the energy level location; and that when the interaction is extremely repulsive the bosons and fermions tend to the same limit. This is related to the Tonk Girardeau limit [8] where the bosons proprieties are similar to the ones for a non interacting fermions (except for the impulsion distribution). It is interesting to notice the decrease of the gap between the first curve l=0 and the curve for l=1 in the extreme repulsion for important ranges in two dimensions, making these two level tending towards being degenerate. This result shows that in this regime the repulsion is able to overcome the amount of the centrifugal potential equivalent to *l=1* corresponding to the next fermionic level. When comparing the results obtained for two dimensions and three dimensions we can notice the regularity with which the levels react to the interaction whether in the fundamental principal states (*n=0*) fig. 4 or the first principal excited states (*n=1*) fig.5, the three dimension being always higher in energy as the centrifugal potential is naturally higher in this case (l_{2d} corresponds to $l_{3d}+1/2$ for the caluculations). We can notice also the same tendency to "degeneracy" for the three first levels (l=0,1,2). The *m* quantum number (projection of *l*) is not relevant for the case of 3 dimensions since the energy is only dependent on (*n*,*l*).

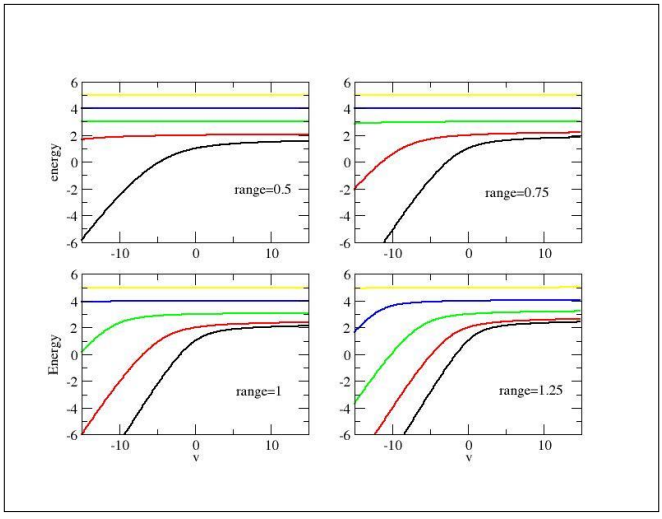

Fig.1. Energy spectrum for the fundamental radial state with increasing value of the angular momentum quantum number (l=0,1,2,3,4 increasingly) in two dimensions. The even value of *l* are for bosons and odd value are for fermions.

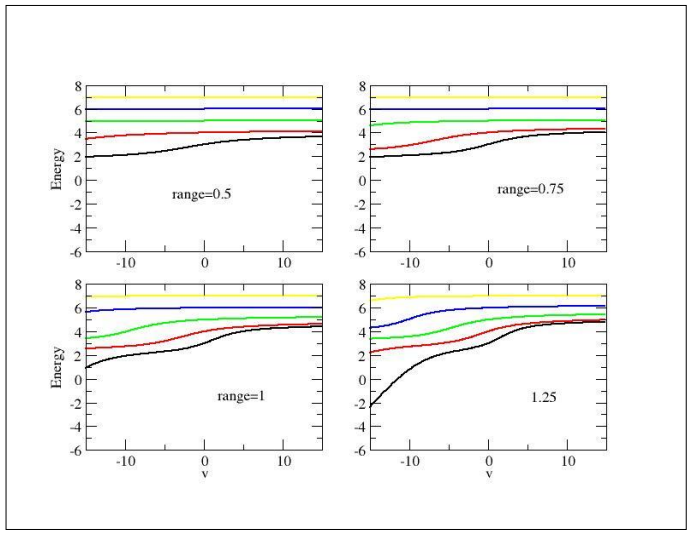

Fig.2. Energy spectrum for the first relative excited state with increasing value of the angular momentum quantum number (l=0,1,2,3,4 increasingly) in two dimensions. The even value of *l* are for bosons and odd value are for fermions.

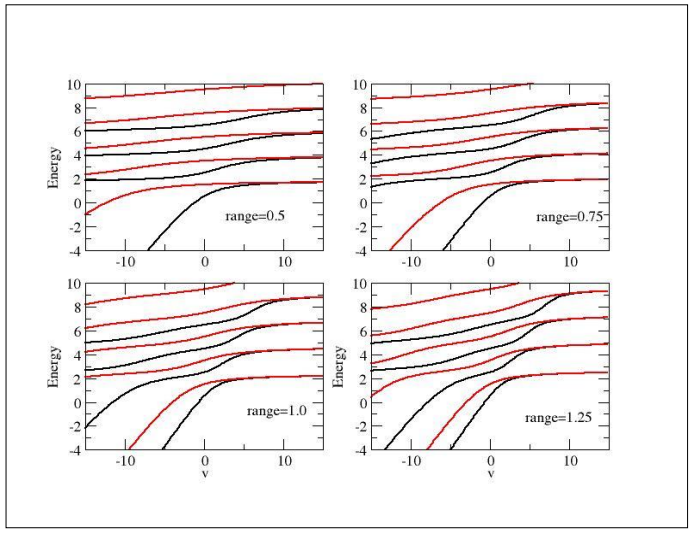

Fig.3. Energy spectrum for the fundamental relative state with increasing value of *n* with even value (black curve) for bosons and odd value(red curve) for fermions in one dimension.

4. Spatial Correlations

Exploiting the wave function derived from the previous calculations it is possible to deduce the probability density distribution as a tool to investigate the possible spatial correlations. In figure 6 we are plotting the radial probability density versus the position *r* for different value of the interaction strength V_0 for a fixed range a=1 and the three figures in one panel are for the three dimensionalities. We want to compare the different dimensionalities for increasing energy states.

In figure 6 the comparison is established for *n=0* and *l=0* where the value of *l* is not degenerate in two and three dimensions and consequently the angular distribution is isotropic . For one dimension we are considering the state with n=0. These states are of bosonic nature (the total wave function is symmetric) which explains the possibility of the two particles to be simultaneously in the same position *r=0 (*center of the trap*)* for one, two and three dimensions where the distributions are quite similar (notice that the 1d results are renormalized to take account of the conversion to polar coordinates). It is interesting to notice that the probability saturates nearly towards the same limit where the repulsion due to the interaction (which is the same in the three cases) is the most dominant player in this regime.

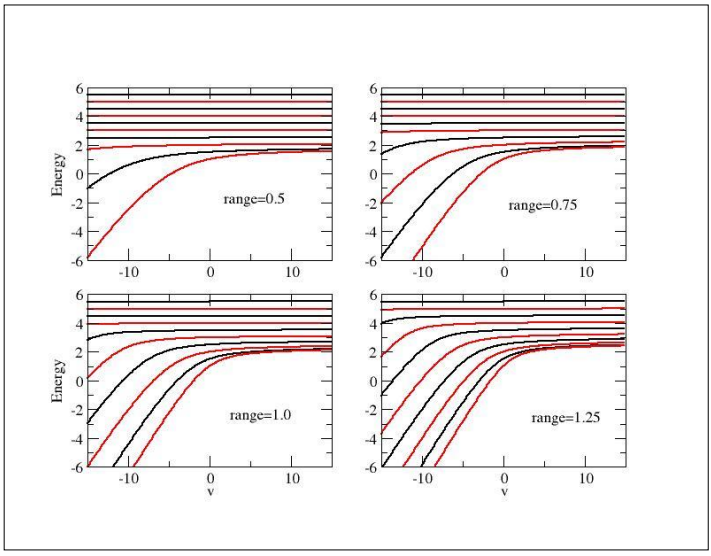

Fig.4. Energy spectrum for the fundamental state (n=0) with increasing value of the angular momentum quantum number (l=0,1,2,3,4) in three (black) and two dimensions (red)

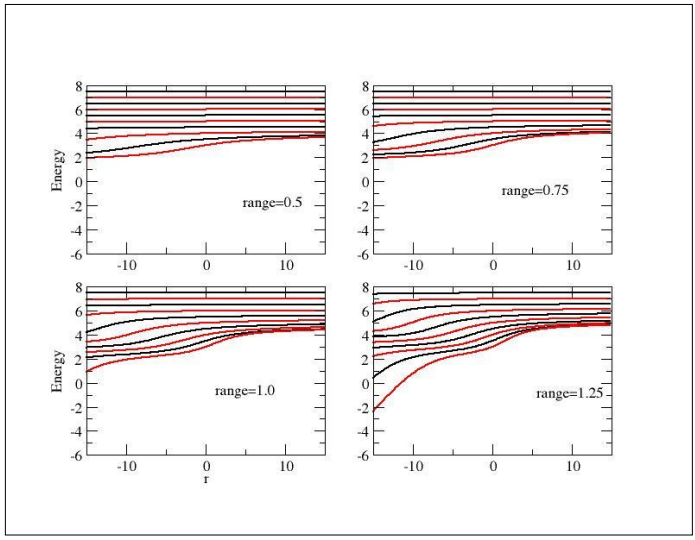

Fig.5. Energy spectrum for the first excited state (n=1) with increasing value of the angular momentum quantum number (l=0,1,2,3,4) in three (black)and two dimensions (red)

We looked also to the radial distribution for higher energy states. We can see on figure 7 the distribution for *n=0* and *l=1* in two and three dimensions and the one for n=1 in one dimension. These distributions are of fermionic nature as the total function is antisymmetric in these cases. It is noticeable on these figures that though the distribution is completely suppressed in the trap center because of the Pauli exclusion principle, the suppression is higher in the case of 3d and 2d because of the centrifugal force. We can also notice that the curves in the attractive part are shifted towards the trap center and that the curve for the repulsive interaction are more repelled from the center as the interaction is acting in the absence of centrifugal potential. The effect of the centrifugal forces increases gradually from two then to three dimensions. For the states n=0 and l=2 in three and two dimensions and n=2 in one dimensions (bosonic states) we have two nodes for the case of one dimension; this makes the comparison less obvious. However it is important to report in this energy regime that at the same time where the distribution is completely suppressed in the center of the trap for three and two dimensions, the two particles are still likely to be found in the center of the trap for one dimension even for the very repulsive interaction (fig.8).

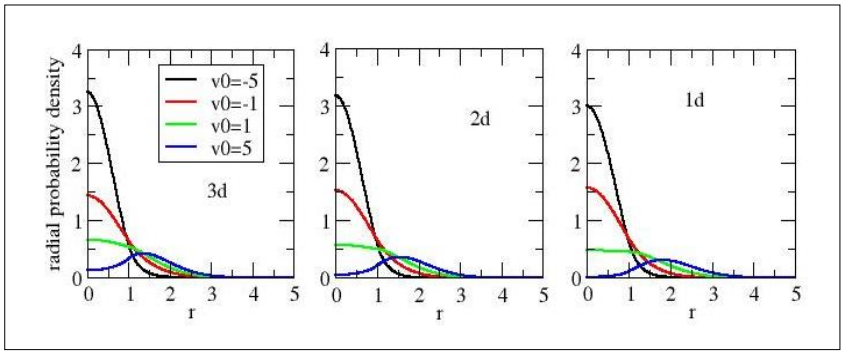

Fig.6. comparison of the ground state normalized radial distribution for (l=0, n=0) in three dimensions, two dimensions and (n=0) for one dimension

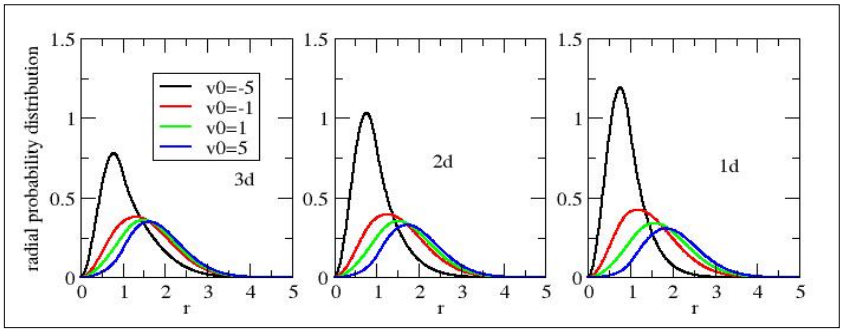

Fig.7. comparison of the normalized radial probability distribution for the states (l=1, n=0) in the three dimensions, two dimensions and (n=1) for one dimension

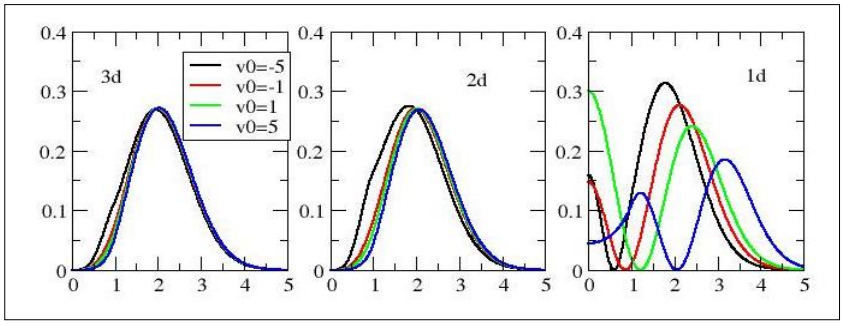

Fig.8. comparison of the normalized radial probability distribution for the states (l=2, n=0) in the three dimensions, two dimensions and (n=2) for one dimension.

5. Conclusion

It was possible by extending the results already established for a simplified step like potential to three dimensions to elaborate a comparative study for the three dimensionalities. This study aimed at singling out the effect of the different dimensionalities in the presence a long ranged interaction for
two particles confined in a harmonic potential. The study shows clearly that the effect is globally related to the centrifugal forces which are in turn dependent on the angular momentum. The effect is more pronounced in three dimensions because of the natural momentum excess from one end and is totally absent in one dimension in the other end. This contribution is a try to comprehend the details of the correlation for bosonic and fermionic systems and shed light on the major players for different energies and interaction regimes. This paper for preliminary results was written in a very compact form, more details and results are to be worked out in a coming publication.

References

[1] D. Blume. Reports on Prog. Phys. **75** (2012) 046401.
[2] J. W. Abraham, M. Bonitz, Contrib. Plasma Phys. **54** (1) (2014) 27-99.
[3] A.V. Turbiner. Physics Reports **642** (2016) 1-71.
[4] H. A. Bethe. Z. Phys. **71** (1931) 205.
[5] T. Busch, B.G. Englert, K. Rzazewski, M. Wilkens. Foundations Phys. **28** (1998) 549–559.
[6] R. Ołdziejewski, W. Górecki, K. Rzążewski. Europhys. Letters **114** (2016) 4.
[7] P. Kościk, T.Sowiński. Scientific Reports **9** (2019) 12018.
[8] M. Girardeau. Journal of Mathematical Physics. ***1** (6) (1960) 516*

Journal of Physical & Chemical Research

Journal homepage:

The on-axis intensity behavior of the diffracted Laguerre-Gaussian beam, LG_p, by an opaque disk

Saoussen Chabou[1*], Abdelhalim Bencheikh[2]

[1]Applied Optics Laboratory, Institute of Optics, and Precision Mechanics, Sétif1 University, Sétif 19000, Algeria.
[2]Department of Electromechanics, Faculty of sciences and technology, University of Bordj Bou Arréridj, BBA 34000, Algeria.

** Corresponding author: Tel./Fax: +213-664-741-888; E-mail address: ch.saoussene@hotmail.com/ chabousaoussene@univ-setif.dz*

Article history
Received March 21, 2022
Accepted for publication April 05, 2022

Abstract

In this work, we present a detailed study of the on-axis intensity distribution of the Laguerre-Gaussian beam with no azimuthal index, diffracted by an opaque disk, by means of numerical simulation of Fresnel-Kirchhoff diffraction integral. We investigate the effect of the opaque disk size, the beam order, the beam waist, and the focal length. The results show that different focal phenomena may occur including the focal shift, focal split, and focal switch.

Keywords: Laguerre Gaussian beam, diffraction, focal shift, focal split, focal switch

1. Introduction

Higher-order Gaussian transverse modes [1] that are solutions of the paraxial Helmholtz wave equation in free space are eigenfunctions of the Fourier transform known as scaled propagation invariant beams. In cylindrical coordinates, the well-known Laguerre-Gaussian (LG) modes, that are characterized by two indices l and p corresponding to the azimuthal and radial indices respectively, play an important role in many different fields of physics and are widely used for various applications such as optical trapping and micro-manipulation [2,3], free-space

communication [4,5], and quantum information [6,7].
For that reason, the propagation properties of such kinds of structured light beams are extensively studied both experimentally and theoretically by researchers in various mediums and through optical systems [8-14].
When investigating the focusing properties of an optical beam, under certain conditions, the maximum intensity of a focused or diffracted field is not located at the geometric focus, but closer to the lens or the diffraction plane. This phenomenon, which is referred to as focal shift, was first found, in 1960, by Goubau [15] and Van Nie [16]. Then in 1980, Wolf and Li [17-19] discussed and explained focal shift for a fundamental Gaussian beam. Since then, due to its theoretical and practical interests, many studies have explored this phenomenon for different classes of beams such as Laguerre-Gaussian beams [20-23], Hermite-Gaussian beams [24], Bessel-Gaussian beams [25,26], Flat-topped beams [27].
Besides the focal shift, a focal switch or focal split can appear, wherein the maximum intensity jump from its position to another or the focus splits into two peaks [28-31].
The knowledge of the beam propagation behavior through optical systems is one of the keystones to getting the desired results. The present work provides a detailed study of the on-axis intensity distribution of Laguerre Gaussian beam, LG_p^0, diffracted by an opaque disk that not addressed before. The influence of different parameters including opaque disk size, radial beam order, beam waist, and focal length, on the on-axis intensity, is examined. Numerical simulations, using the Fresnal-Kirchhoff diffraction integral, show that such parameters can significantly affect the maximum intensity position, which plays an important role in some applications.

2. Focal phenomena of diffracted Laguerre Gaussian beam by an opaque disk

Consider a cylindrical LG beam with no azimuthal index ($l = 0$) is expressed, at the waist plane$z = 0$, as follows

$$u_{in}(\rho, z = 0) \propto L_p\left(2\frac{\rho^2}{w^2(z)}\right) exp\left(-\frac{\rho^2}{w^2(z)}\right) \quad (1)$$

where $w^2(z) = w_0^2[1 + (z/z_R)^2]$ is the beam width, $z_R = \pi w_0^2/\lambda$ is the Rayleigh length, w_0 is the Gaussian waist radius, and L_p is a Laguerre polynomial of order p. p dark nodal rings.

From the Fresnel-Kirchhoff diffraction theory, the propagated electric field at a distance z is given by [32]

$$u_{out}(r,z) = \int_0^\infty u_{in}(\rho, z=0)\tau(\rho)J_0\left(\frac{2\pi}{\lambda z}r\rho\right)exp\left[\frac{i\pi\rho^2}{\lambda}\left(\frac{1}{z}-\frac{1}{f}\right)\right]\rho d\rho \quad (2)$$

where r is the radial distance to the propagation axis, J_0 is the Bessel function of order zero, and $\tau(\rho)$ is the transmittance functions.

$$\tau(\rho) = \begin{cases} 0 & \rho \le a \\ 1 & \rho > a \end{cases} \quad (3)$$

with a is the radius of the opaque disk.

The transverse intensity of an LG beam of order $\boldsymbol{l = 0}$, $\boldsymbol{p = 5}$ is displayed in figure 1. The p dark nodal rings in the cross-sectional on the right indicate the zeros of the beam's intensity, clearly seen on the left.

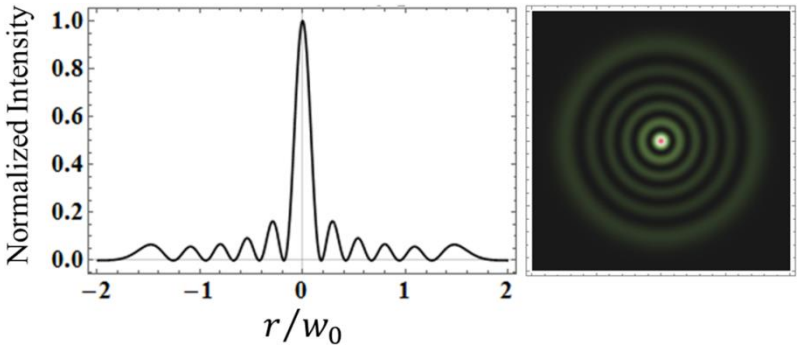

Figure 1. The transverse (on the left) and cross-sectional (on the right) intensity profile of $\boldsymbol{LG}$ beam with $\boldsymbol{p = 5}$ and $\boldsymbol{l = 0}$.

3. Results

In this section, we investigate the on-axis intensity distributions of the diffracted Laguerre-Gaussian beam, LG_p, under conditions of different opaque disk size a/w_0, different radial beam order p, different beam waist w_0, and different focal length f, with $\lambda = 0.0006328\ mm$.

3.1 Different opaque disk sizes:

Figure 2 shows the on-axis intensity behavior of focused LG beam of radial order $p = 5$ (the un-diffracted case) in figure.2(a), and that of the diffracted one by an opaque disk of different sizes in figure.2(b)-(f). It can be seen, from figure.1(a), that there is only one intensity peak located at $z_0 = 240.8\ mm$, a little away from the geometric focal plane. For figure.2(b)-(e), in the presence of opaque disk of different sizes (corresponding to the first, second, third, and fourth zeros intensity), one focal spot changes remarkably into multiple intensity peaks. This

phenomenon is accompanied by a permutation of the focal point, in which the maximum intensity jumps from one position to another position. It can be also noticed that the maximum intensity peak shifts from the geometrical focus moving toward the lens and the opaque disk. In figure.2(f), when the whole beam is blocked, it is shown that the axial intensity becomes only one maximum peak, which is also located before the geometrical focus.

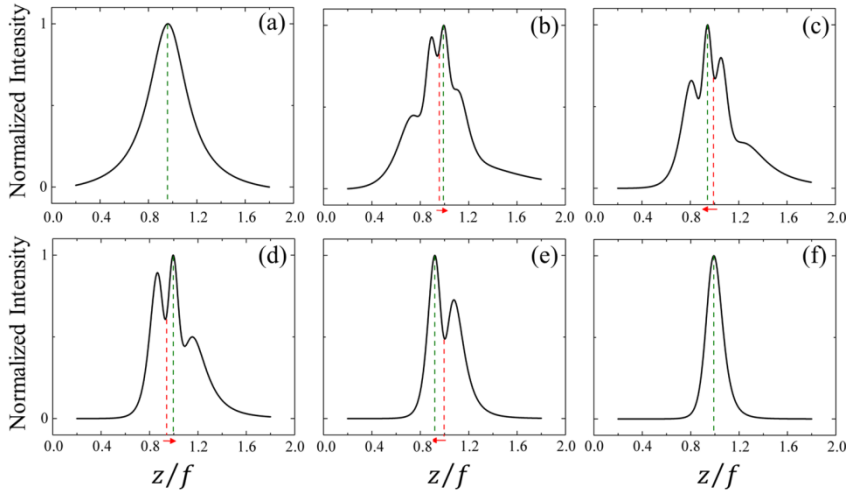

Figure 2. The on-axis intensity distribution of $\boldsymbol{LG}$ beam diffracted by an opaque disk, with $\boldsymbol{p = 5, w_0 = 0.5\,mm, f = 250\,mm}$, for different opaque disk sizes $\boldsymbol{a/w_0}$ that were chosen to coincide with the zeros of the beam's intensity.

3.2 Different radial beam order:

Figure 3 displays how the on-axis intensity distribution of the diffractedLG beam by an opaque disk is affected when varying the beam order p. For all the beam orders, a slightly focal shift occurs with showing a focal split accompanied by a focal switch in some cases such as figure.3(b) and (d).

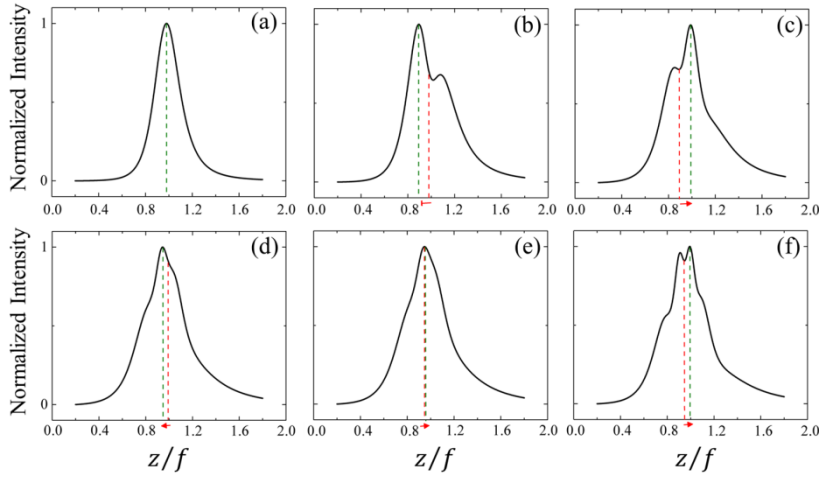

Figure 3. The on-axis intensity distribution of $\boldsymbol{LG}$ beam diffracted by an opaque disk, with $\boldsymbol{a/w_0 = 0.3, w_0 = 0.5\,mm, f = 250\,mm}$, for different radial beam order $\boldsymbol{p = 1, 2, 3, 4, 5, 6}$, respectively.

3.3 Different beam waist:

Figure 4 illustrates the effect of the beam waist on the on-axis intensity behavior of the diffracted *LG* beam by an opaque disk. It can be seen that for $w_0 > 0.5$, the maximum intensity peak keeps the same position.

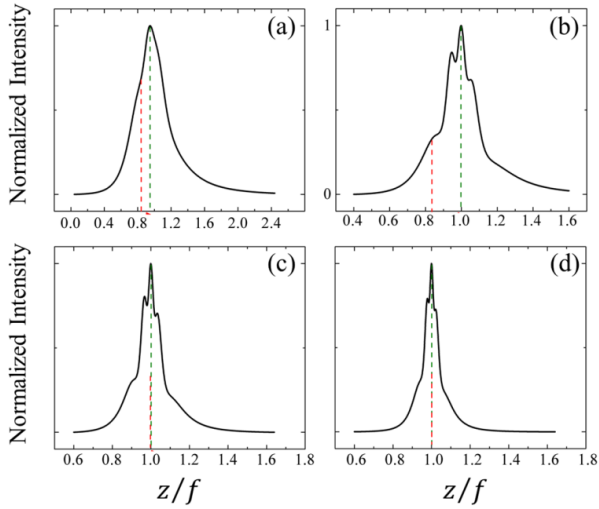

Figure 4. The on-axis intensity distribution of $\boldsymbol{LG}$ beam diffracted by an opaque disk, with $\boldsymbol{a/w_0 = 0.3, p = 5, f = 250\,mm}$, for different beam waist $\boldsymbol{w_0 = 0.5, 0.7, 0.9, 1.1\,mm}$, respectively.

3.4 Different focal length:

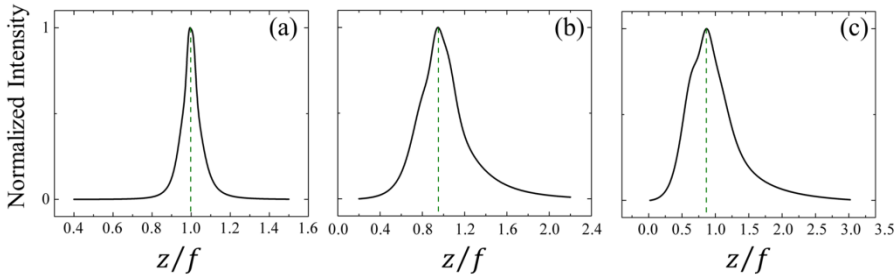

Figure 5. The on-axis intensity distribution of $\boldsymbol{LG}$ beam diffracted by an opaque disk, with $\boldsymbol{a/w_0 = 0.3, p = 5, w_0 = 0.5\ mm}$, for different focal length $\boldsymbol{f = 50, 250, 500\ mm}$, respectively.

Figure 5 exhibits the on-axis intensity behavior of the diffracted *LG* beam, by an opaque disk, when the lens is changed. It can be seen that the lens of the small focal length (figure.5(a)) gives a closer position to the geometrical focus of maximum intensity peak.

3.5 Focal shift evolution:

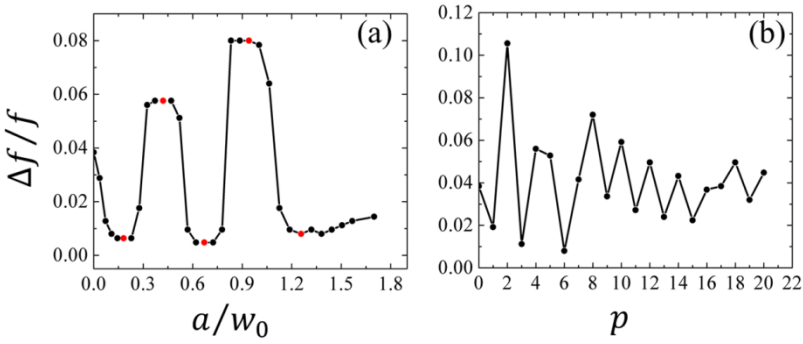

Figure 6. The focal shift variation, of the diffracted $\boldsymbol{LG}$ beam by an opaque disk, as a function of (a) the opaque disk size and (b) the beam order. $\boldsymbol{\Delta f = f - z_0}$, where $\boldsymbol{f}$ is the geometric focal length and $\boldsymbol{z_0}$ is the corresponding plane to the maximum intensity.

Figure 6 shows how the focal shift varies under different opaque disk sizes (figure.6(a)) and different beam orders (figure.6(b)). From figure.6(a), the amount of the focal shift oscillates between a min and max value, which is maybe due to the focal switch. The red points indicate that the focal switch occurs. In figure.6(b), in general, the focal shift of the even orders is larger than that of the odd orders.

4. Discussion

From the results, it is found that the on-axis intensity distribution of an LG beam diffracted by an opaque disk exhibits a focal shift accompanied by a focal split and focal switch. It's well known that the focal shift effect depends strongly on the Fresnel number of the system, and since the opaque disk doesn't limit the beam size thus the Fresnel number keeps the same, in contrast to the truncated case. Although, the focused beam without an obstacle also exhibits a slight focal shift, the same as the case of the opaque disk. Even it is negligible but the precise position of the maximum intensity has a crucial role for some applications. The present work has discussed the influence of different parameters on the on-axis intensity behavior, of the LG beam diffracted by an opaque disk, including the position of the maximum intensity.

5. Conclusion

In summary, using the Fresnel-Kirchhoff diffraction integral, we have studied, numerically, the intensity distribution of diffracted Laguerre-Gaussian beam, LG_p, by an opaque disk, along the longitudinal direction. We have explored how the on-axis intensity is affected when altering the opaque disk size, the beam order, the beam waist, and the focal length. The simulation results show that the maximum intensity peak can shift along the optical axis or split into multi peaks or jump from its position. These results help us to understand and control the intensity distribution along the axis.

References

[1] A.E. Siegman, Lasers, University Science Books: Mill Valley, CA, (1986).
[2] A. D. Kiselev, D. O. Plutenko. Physical Review A **94** (2016) 013804.
[3] V. Garbin, D. Cojoc, E. Ferrari, R. Z. Proietti, S. Cabrini, and E. Di Fabrizio. Japanese journal of applied physics **44** (2005) 5773.
[4] A. Trichili, A. B. Salem, A. Dudley, M. Zghal, and A. Forbes. Opt. Lett **41** (2016) 3086–3089.
[5] G. Gibson, J. Courtial, M. J. Padgett, M. Vasnetsov, V. Pas'ko, S. M. Barnett, and S. Franke-Arnold. Opt. Express (2004) 5448–5456.
[6] A. Schutza. McNair Scholars Journal **14** (2010) 8.
[7] L. Marrucci, E. Karimi, S. Slussarenko, B. Piccirillo, E. Santamato, E. Nagal, and F. Sciarrino. Journal of Optics **13** (2011) 064001.
[8] H.T. Eyyuboğlu, Y. Baykal, A. Falits. Appl. Phys. B **104** (2011) 1001–1006.
[9] D.DENG, Q.GUO. Journal of Optics A: Pure and Applied Optics **10** (2008) 035101.
[10] M. Newstein, B. Rudman. IEEE journal of quantum electronics **23** (1987) 481-482.
[11] M. Yu, Y. Han, Z. Cui, and H. Sun. JOSA A **35** (2018) 1504-1510.

[12] S. Chabou, A. Bencheikh, J. Pinnell, V. Rodrí guez-Fajarda, and A. Forbes. Applied Physics B **126** (2020) 1-12.
[13] J. Pinnell, V. Rodrí guez-Fajarda, A. Forbes, S. Chabou, K. Mihoubi, A. Bencheikh. Physical Review A **102** (2020) 033524.
[14] A. Bencheikh, S. Chabou, O.C. Boumeddine. JOSA A **37** (2020) C20-C26.
[15] G. Goubau. "Optical relations for coherent wave beams," in Electomagnetic Theory and Antannas, vol 2, E. C. Jordan, ed., Macmillan Co: New York (1963)
[16] A. Van Nie. Philips Res. Rep **19** (1964) 378–394.
[17] Y. Li, E. Wolf. Opt. Commun **39** (1981) 211–215.
[18] Y. Li, E. Wolf. J. Opt. Soc. Am. A **1** (1984) 801–808.
[19] Y. Li, E. Wolf. Opt. Commun. **42** (1982) 151–156.
[20] W. H. Carter, M. F Aburdene. J. Opt. Soc. Am. A **4** (1987) 949–1952.
[21] Z.C. Ren, S.X. Qian, C. Tu, Y. Li, H.T. Wang. Optics Communications **334** (2015) 156-159.
[22] M. Zhang, Y. Chen, L. Liu, Y. Cai. Journal of Modern optics **63** (2016) 2226-2234.
[23] Y. Chen, S. Huang, M. Chen, X. Liu. JOSA A **35** (2018) 1585-1591.
[24] B. Lu, R. Penga. Optics & Laser Technology **35** (2003) 435-440.
[25] B. Lü, W. Huang. Opt. Commun **109** (1994) 43-46.
[26] X. Ji, B. Lü. Opt. Laser Technol **39** (2007) 562–568.
[27] R. Borghi, M. Santasiero, S. Vicalvi. Opt.Commun **154** (1998) 243-248.
[28] B. Lü, R. Peng. Journal of Optics A: Pure and Applied Optics **4** (2002) 601.
[29] X. Gao, J. Li. Optics communications **273** (2007) 21-27.
[30] M. Martines-Corral, V. Climent, Appl. Opt **35** (1996) 24.
[31] Y. Li. J. Opt. Soc. Am. A **14** (1997) 1297.
[32] M. Born, E. Wolf, Principles of optics: electromagnetic theory of propagation, interference and diffraction of light, Elsevier (2013).

Journal of Physical & Chemical Research

Journal homepage:

Vector flat-top beam with Higher-order

Madjeda Kherif[1], Assia Yousfi[1], Abdelhalim Bencheikh[1,2*], Saoussene Chabou[1], Abdeldjalil Benstiti[1], Ouis Chouaib Boumeddine[1]

1Applied optics laboratory, Institute of optics and precision mechanics, University Ferhat Abbas Setif 1, Setif 19000, Algeria
2 Department of Electromechanics, Faculty of sciences and technology, University of Bordj Bou Arréridj, BBA 34000, Algeria

** Corresponding author: Tel./Fax:+213671403172; E-mail address: Madjeda.kherif@gmail.com; Madjeda.kherif@univ-setif.dz*

Article history
Received March 22, 2022
Accepted for publication April 04, 2022

Abstract

In this paper, we introduce a new kind of vector flat-top-laser beam; we call it higher-order vector flat-top beam. We generate such laser beam, by the incoherent superposition of two orthogonal modes in polarization (Horizontal and vertical polarizations). The two basic modes are; the fundamental-Gaussian beam (LG_{00}) and one Higher-order-Vortex-Laguerre-Gaussian beam ($LG_{0\ell}$) with different topological charges of ($\ell = 1, \ell = 2,$ and $\ell = 3$). The resulting beam has almost a uniform intensity, and it is invariant under propagation in lossless systems. We believe that the resulting laser beam will have applications in laser material processing and laser micromachining.

Keywords: Vector beams, Flat-top beams, Laguerre-Gaussian beams

1. Introduction

Recently, the possibility of structuring light, both in scalar and vector regimes, in its spatial degrees of freedom such as polarization, phase, and amplitude [1] has opened a new way towards the development of laser applications. A most common case is transforming the Gaussian beam that has a peak intensity into uniform irradiance known as flat-top beam. The latter offers many applications including optical data processing [2,3], optical trapping [4], gravitational-waves detectors [5], laser-driven acceleration of particles [6, 7], optical recording, medical surgery, laser material processing, laser coupling into fibres [2], and military use [8].

Thus, a range of generation methods for this beam has been introduced such as diffractive optical elements [9], aspherical refractive lenses [10], and micro-lens arrays [11]. The traditional flat-top beam alters its shape during the propagation in contrast to the higher-order-Gaussian beams, which are eigenmodes of free space [12]. Among which, are the well-known Laguerre-Gaussian beams, which are characterized by a radial and azimuthal index. Besides scalar beams, the light beams with spatially inhomogeneous states of polarization known as vector beams [2] have attracted lots of interest in various fields by offering new groundbreaking applications.

In this work, we present a higher-order flat-top beam with variant polarization, by superposing the fundamental-Gaussian beam LG_{00} and Laguerre-Gaussian-vortex beam $LG_{0\ell}$ with different topological charges ($\ell = 2$; $\ell = 3$) that could exhibit a uniform intensity during the propagation. We use simulations, to emphasize the main characteristics of the obtained higher-order-vector flat-top beams.

2. Superposition of a Gaussian beam (LG_{00}) with a first-order-vortex beam (LG_{01})

Firstly, in this section, we present the principle of the generation of a Vector flat-top beam, as demonstrated by the authors of the paper [13]. In that paper, they used a weighting superposition of a Gaussian beam and the first-order-Vortex-Laguerre-Gaussian beam. The amplitude of the orthogonal superposition is given by

$$E(r,\varphi,z) = \sqrt{\alpha}\ LG_{00}(r,\varphi,z)\hat{e}_V + \sqrt{(1-\alpha)}LG_{01}(r,\varphi,z)\hat{e}_H \qquad (1)$$

With $\hat{e}_V$ and $\hat{e}_H$ are polarization vectors, they denote the horizontal and vertical components of the Jones matrix. α is a parameter that quantifies the vectorness degree of an optical beam given by $V = 2|\sqrt{(\alpha(1-\alpha)\,)}|$, where, for a perfect flat-top beam $\alpha = 0{,}5$, and we expect a perfect vector state with $(V = 1)$. However, for $\alpha = 0$ or $\alpha = 1$ the beam becomes purely scalar.

From equation (1), the intensity of the resulting beam is

$$I(r,\varphi,z) = \alpha|\ LG_{00}(r,\varphi,z)|^2 + (1-\alpha)\,|LG_{01}(r,\varphi,z)|^2 \qquad (2)$$

Where $LG_{01}(r,\varphi,z)$ and $LG_{00}(r,\varphi,z)$ refer to Laguerre-Gaussian modes of a radial order $p = 0$ and azimuthal orders $\ell = 1$ and $\ell = 0$ respectively.

The amplitude expression of the normalized $LG_{0\ell}\,(r,\varphi,z)$ mode is expressed by

$$LG_{0\ell}\,(r,\varphi,z) = \sqrt{\frac{2}{\pi\, w(z)|\ell|!}}\left(\frac{\sqrt{2}r}{w(z)}\right)^{|\ell|} exp\left(-\frac{r^2}{w(z)^2} + ik\frac{r^2}{2R(z)}\right) \times \exp\big(i(1+|\ell|)\eta(z)\big) \qquad (3)$$

Here; $w(z) = w_0\sqrt{1 + \left(\frac{z}{z_r}\right)^2}$, $R(z) = z\left(1 + \left(\frac{z_r}{z}\right)^2\right)$, $z_r = \pi w_0^2 / \lambda$, $\eta(z) = \arctan\left(\frac{z}{z_r}\right)$, $\theta_0 = (\lambda/\pi w_0)$, are, the beam width, the ray of wavefront curvature, the Rayleigh length, the Gouy phase shift, and the divergence angle, respectively. In addition, w_0 is the Gaussian beam waist, λ is the wavelength of the used laser.

As a first example, we show in Figure 1, the 3D intensities representation of the fundamental-LG beam (Fig1. a), as well as the first-order-vortex-LG beam (Fig1.b). The incoherent superposition of the cited beams gives us the first-order-vector flat-top beam (Fig1.c). In subfigure (Fig1.d) we present the propagated flat-top Vector beam in 3D. The main conclusion is, the invariant property of the obtained beam during propagation. It is worth recalling the different numerical values used in the different simulations; the beam waist is w_0=1mm, and the laser wavelength is λ=532 nm.

3. Superposition of Gaussian beam (LG_{00}) with a higher-order-vortex ($LG_{0\ell}$) beam

Following the same principle presented above, we demonstrate in this section the generation of higher-order vector flat-top beam, by the superposition of one higher-order-LG beam with fundamental-Gaussian beam. We have the same equation of the resulted intensity, it is given by

$$I(r,\varphi,z) = \alpha|\ LG_{00}(r,\varphi,z)|^2 + (1-\alpha)\ |LG_{0\ell}(r,\varphi,z)|^2 \qquad (4)$$

In the following, we use subsections to present results of each superposition order.

3.1 Superposition of a fundamental-Gaussian Beam (LG_{00}) with a Higher-order-vortex (LG_{02}) Beam

Let's consider at first stage the superposition of the second-order-Vortex-LG beam with the fundamental-Gaussian beam, the profiles as well as 3D presentation of the different beams are presented in Figure 2

3.2 Superposition of a fundamental-Gaussian Beam (LG_{00}) with a Higher-order-vortex (LG_{03}) Beam

Let's now consider the superposition of the third-order-vortex-LG beam with the fundamental-Gaussian beam, the profiles as well as 3D presentation of the different beams are presented in Figure 3

4. Results

In this section, we simulate intensities of the generated vector flat-top beams using equations (1- 4)

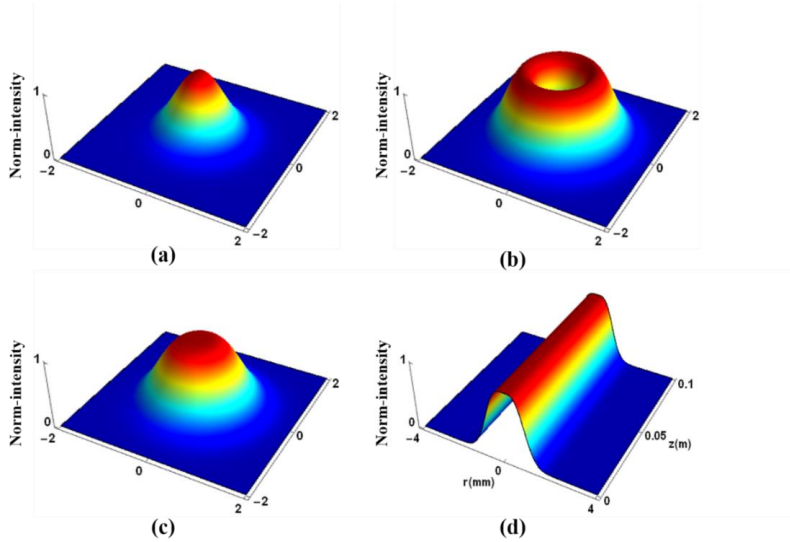

Figure 1. Intensity profiles 3D view; (a) fundamental-Gaussian beam with a peak at the center, (b) first-order-Laguerre-Gaussian-Vortex beam, (c) superposition of fundamental-Gaussian beam (a) and first-order of Laguerre-Vortex beam (b), (d) propagation of first-order-flat-top beam.

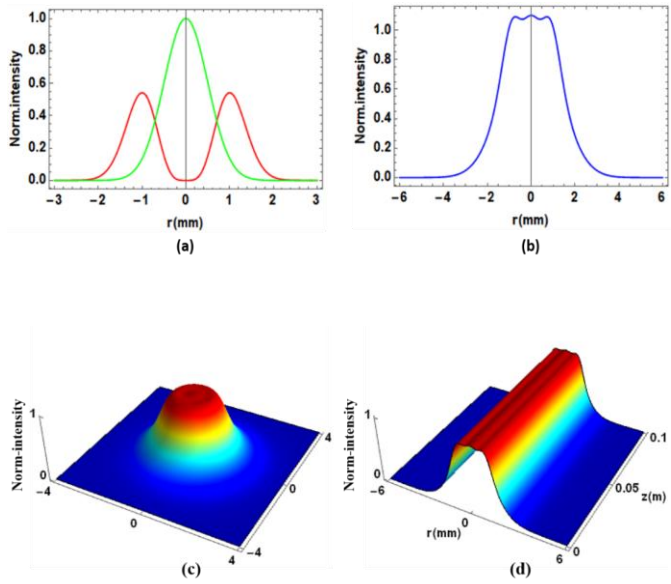

Figure 2. Intensity distribution. (a) The fundamental-Gaussian beam (LG_{00}) shown in green and second-order-vortex-Laguerre-Gaussian beam (LG_{02}) shown in red; (b) The total intensity distribution of the superposition of (LG_{00}) with (LG_{02}). (c) 3D view of the Intensity distribution of the obtained flat-top beam (d) The propagation of a flat-top beam produced by superposition of (LG_{00}) with (LG_{02}).

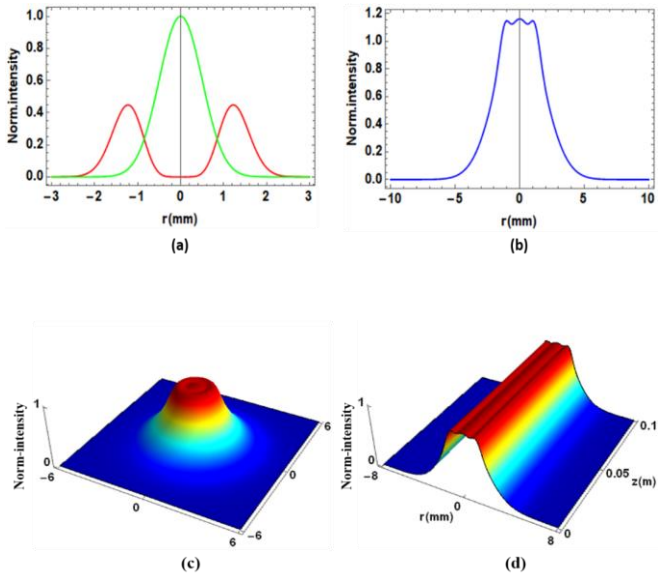

Figure 3. Intensity distribution. (a) The fundamental-Gaussian beam (LG_{00}) shown in green and third-order-vortex-Laguerre-Gaussian beam (LG_{03}) shown in red; (b) The total intensity distribution of the superposition of (LG_{00}) with (LG_{03}) . (c) 3D view of the Intensity distribution of the obtained flat-top beam (d) The propagation of a flat-top beam produced by superposition of (LG_{00}) with (LG_{03}).

5. Discussion

From the obtained results and figures (1-3), it is clear that the superposition of a Vortex-LG beam having a doughnut shape, with a Gaussian beam having a pic shape, the created beams are of a flat shape. The quality of the flat shape depends strongly on the LG beam order. The bigger is the LG beam order; the better is the quality of the beam flatness. It is worth to mention, that using higher-order-LG beams, requires the modification of the fundamental-Gaussian beam waist.

6. Conclusion

In summary, we have demonstrated a technique to create a vector flat-top beam using the superposition of, one higher-order-Vortex-LG beam and a fundamental-Gaussian beam. The two beams are orthogonal in polarization. By changing the order of the LG-vortex beam, as well as the width of the Gaussian beam, one can change the flatness of the obtained beams. Consequently, we can provide a multiple Vector flat-top beams with different characteristics, which can be used in many applications, such as High-resolution microscopy, micromachining and optical tweezing.

References

[1] A. Forbes. Laser. Photon. Rev **13.11** (2019) 1900140-19.
[2] Q. Zhan. Adv. Opt. Photon. **1** (2009) 1-57.
[3] R. E. Grojean, D. Feldman, J. F. Roach. Rev. Sci. Instr. **51** (1979) 375-376.
[4] C. Zhao, Y. Cai, X. Lu, and H. T. Eyyuboglu. Opt. Express. **17** (2009) 1753-1765.
[5] S. Gras, D. G. Blair, and L. Ju. Phys. Rev. D **81** (2010) 042001-14.
[6] W. Wang, P. X. Wang, Y. K. Ho, Q. Kong, Y. Gu, and S. J. Wang. Rev. Sci. Instr. **78** (2007) 093103-5.
[7] C. Maher-McWilliams, P. Douglas and P. F. Barker. Nature Photon. **6** (2012) 386-390.
[8] S. Saghafi, M. J. Withford, Z. Ghoranneviss. Canad. J. phy. **84.3** (2006) 223-240.
[9] W. B. Veldkamp. Rev. Sci. Instrum. **53** (1982) 294-297.
[10] S. Zhang. J. Opt. **A 9** (2007) 945-950.
[11] L. S. Weichman, F. M. Dickey, R. N. Shagam. In Solid State Lasers IX, SPIE (2000).
[12] F. Wang, Y. Cai, H. T. Eyyuboğlu, Y. Baykal. In Atmospheric and Oceanic Propagation of Electromagnetic Waves IV. International Society for Optics and Photonics (2010).
[13] B. Nkosi, C. Rosales-Guzman, A. Forbes. App. Opt **57.19** (2018) 5451-5458.

Journal of Physical & Chemical Research

Journal homepage:

Superoxide Anion Radical Interaction With New Quinoline Compounds Measured By Cyclic Voltammetry

Khaoula Douadi[1], Kaabi Ilhem[1*], Tahar Douadi[1], Mousa Al-Noaimi[2], Salah Chafaa[1]

[1] Laboratory of Electrochemical of Molecular Materials and Complex LEMMC. Department of Process Engineering, Faculty of Technology, University Ferhat ABBAS Setif -1, Sétif, 19000, Algeria..
[2] Department of Chemistry, Hashemite University, P.O. Box 150459, Zarqa 13115, Jordan.

** Corresponding author: Tel./Fax: +213-698-01-07-78; E-mail address: kaabi.ilhem@univ-setif.dz.*

Article history
Received March 10, 2022
Accepted for publication March 24, 2022

Abstract

Cyclic voltammetry was used to study the interaction of four quinoline derivatives with superoxide anion radical ($\boldsymbol{O_2^{\cdot -}}$). This method is based on the decrease of the anodic peak current of the superoxide anion radical $\boldsymbol{O_2^{\cdot -}}$generated electrochemically by the reduction of molecular oxygen $\boldsymbol{O_2}$ dissolved in acetonitrile. The results obtained reveal that all derivatives showed a higher antioxidant activity than the standard used BHT. The binding parameters of the studied compounds were estimated in terms of binding constant ($\boldsymbol{k_b}$), ratio of Binding Constants (K_{Red}/K_{Ox}) and binding Gibbs free energy ($\Delta G°$). From the results, it appears that the binding constant kb of the tested compounds is very high ranged from 15922 to 26181 L.mol^{-1} while negative values of $\Delta G°$ indicate the spontaneity of the antiradical reaction. It was also found that interaction of the reduced form $\boldsymbol{O_2^{\cdot -}}$with all derivatives is stronger than the oxidized form $\boldsymbol{O_2}$ with ratio of binding constants values in the range 1.21-159.

Keywords: Quinoline derivative; Superoxide radical $\boldsymbol{O_2^{\cdot -}}$; Cyclic voltammetry; Binding parameters.

1. Introduction

Quinoline derivatives are among the classical divisions of organic chemistry that have been widely studied in different fields of chemistry, including the chemical and pharmaceutical industries [1]. They are

excellent precursors in the synthesis of new systems that may present interesting biological properties related to the treatment of malaria, cardiovascular diseases, antifungal, anti-inflammatory, antibiotic, antitumor and antimicrobial [2–5]. They have shown a favorable pharmacological profile and a confirmed bactericidal power on sensitive strains. They are also used as corrosion inhibitors [1, 6, 7]. Several studies have shown that quinoline derivatives have a significant antioxidant activity and are able to scavenge several free radicals in vitro [8–11]. The present study aimed to determine electrochemically the binding parameters of a series of quinoline compounds having the formula {L= $RC_6H_4NHN=C(COCH_3)$ NHC_9H_6N, X= H, Br, F, NO_2} with superoxide anion $O_2^{\cdot -}$ radicals.

2. Experimental

2.1. Chemicals and reagents

All chemicals were purchased from Sigma-Aldrich and used without purification. Acetonitrile was used as solvent, tetrabutylammonium hexafluorophosphate ($TBuNPF_6$) was used as supporting electrolyte and its concentration was kept 0.1 $mol.L^{-1}$.

2.2. Synthesis

The four target compounds were synthesized according to the procedure described by M. El-Noaimi et al [12] by reacting an appropriate hydrazonyl chloride solution with 8-aminoquinoline and triethylaminel, scheme. 1.

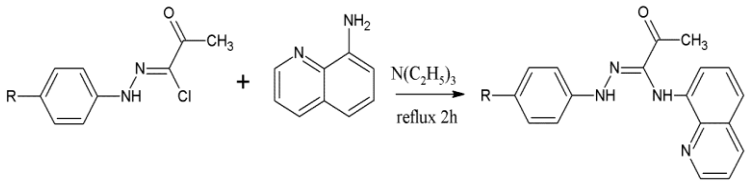

Scheme 1. Synthesis of $RC_6H_4NHN=C(COCH_3)$ NHC_9H_6N compound, H_2L-H: X= H,H_2L-Br: X=Br, H_2L-F: X= F, H_2L-NO_2: X= NO_2.

2.3. Scavenging Activity of Superoxide Anion $O_2^{\cdot -}$ radicals

The Electrochemical measurements were carried by a Voltalab 40 model PGZ301 (Radiometer Analytical) potentiostat / galvanostat) connected to an electrochemical cell with three electrodes. Saturated calomel electrode (SCE) as a reference electrode, a platinum wire as the counter electrode and a glassy carbon electrode (GCE) with a diameter of 2 mm as a working electrode. The potentiostat is piloted by a microcomputer with Volta Master 4 software, version 7.08. All measurements were carried

out at room temperature.

The in situ generation of $O_2^{\cdot -}$ was performed by the reduction of acetonirile solution of commercial molecular oxygen containing 0.1 mol.L^{-1} $TBuNPF_6$ at scan rate 100 mV.s^{-1}, in a potential window from -1.5 to 0.0 V. The superoxide radical scavenging activity is checked by successive addition of 0.1 ml of the solution of each compound, the voltammograms are then recorded under the same experimental conditions.

3. Results and discussion

3.1. Voltammetric Studies of H_2L-R– $O_2^{\cdot -}$ Interaction

Cyclic voltammetry is a useful method to generate $O_2^{\cdot -}$ without an enzyme system and to study its interaction with a molecule or extract, provided that the substrate is not active in the potential oxygen reduction range. The decrease of the anodic peak current of the radical $O_2^{\cdot -}$ with varying concentration of quinoline compounds was exploited to calculate the binding constant, whereas the shift of the peak potential was used to determine the modes of interaction [13,14]. Addition of first volume of all quinoline compounds causes a marked decrease of the anodic and cathodic peak currents accompanied by a shift in the peak potential **(Figure 1)**. The reason of the peak current decrease is that both apparent diffusion coefficient and concentrations of superoxide anion radical are decreased due to the formation of $H_2L - X - O_2^{\cdot -}$ complex [15].

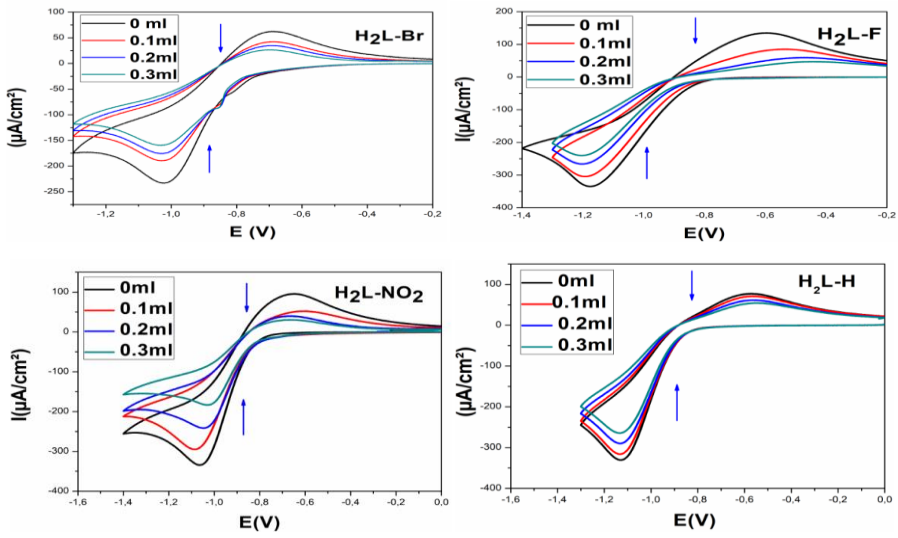

Figure 1. Cyclic voltammograms showing the scavenger effect of the $O_2^{\bullet -}$ radical recorded in the presence of different volumes of H_2L-Br, H_2L-H, H_2L-F and H_2L-NO_2

3.2. Scavenging activity and determination of IC50 values

The percent superoxide anion inhibition of the compounds studied is calculated using the following equation [16]:

$$\%\ O_2^{\cdot -}\ radical\ scavenging\ actuvity = \frac{I_{pa}^0 - I_{pa}}{I_{pa}^0} \times 100 \quad (1)$$

Where $\boldsymbol{I_{pa}}$ and $\boldsymbol{I_{pa}^0}$ present the oxidation peak current densities of $\boldsymbol{O_2^{\cdot -}}$ in the presence and absence of the test compound, respectively. As shown in **Table 1**, the radical scavenging activity towards superoxide anion radicals increases with increasing the concentration.

Table 1. Percentage values of superoxide radical inhibition for H_2L-Br, H_2L-F, H_2L-H and H_2L-NO_2.

Compound	Additionnel volume (ml)	C (mol.L^{-1})	Current I_{pa} (µA)	*RSA* $_{O2\bullet-}$ *%*
H_2L-H	0	/	220.803	/
	0.1	9.9×10^{-6}	218.751	0929
	0 .2	1.94×10^{-5}	209.685	5.035
	0.3	2.83×10^{-5}	193.341	12.437
H_2L-F	0	/	225.442	/
	0.1	9.9×10^{-6}	208.654	7.446
	0 .2	1.94×10^{-5}	180.759	1.820
	0.3	2.83×10^{-5}	151.987	32.582
H_2L-Br	0	/	220.803	/
	0.1	4.34×10^{-5}	110.785	49.825
	0.2	4.95×10^{-5}	105.025	52.434
	0.3	5.46×10^{-5}	99.549	54.914
H_2L-NO_2	0	/	227.527	/
	0.1	9.9×10^{-6}	192.512	15.3892
	0.2	1.94×10^{-5}	168.414	25.980
	0.3	3.63×10^{-5}	131.849	42.051

The IC_{50} values for all molecules were calculated by the plot of the percentage superoxide anion inhibition (% I) versus the molar concentrations (C) (**Figure 2**). The IC_{50} values obtained are shown in **Figure 3**.

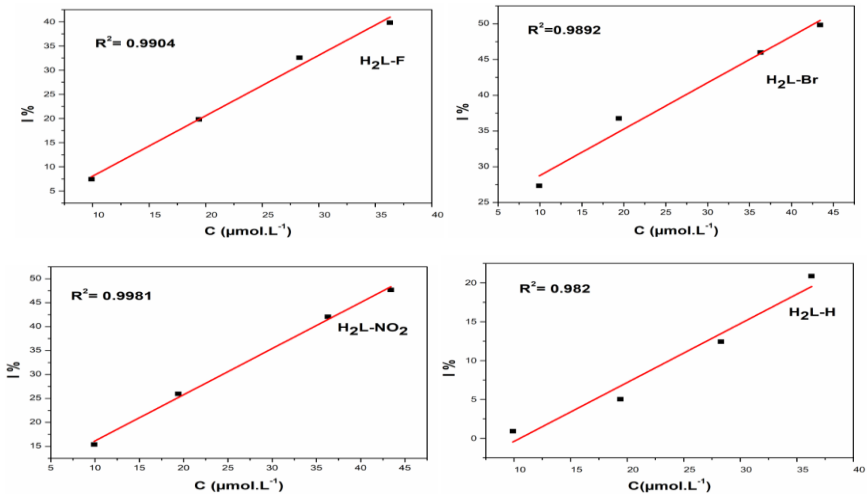

Figure 2. Plot of the ratio of percentage inhibition I % versus the concentration C of compounds H_2L-Br, H_2L-H, H_2L-F and H_2L-NO_2 for the calculation of the IC_{50}

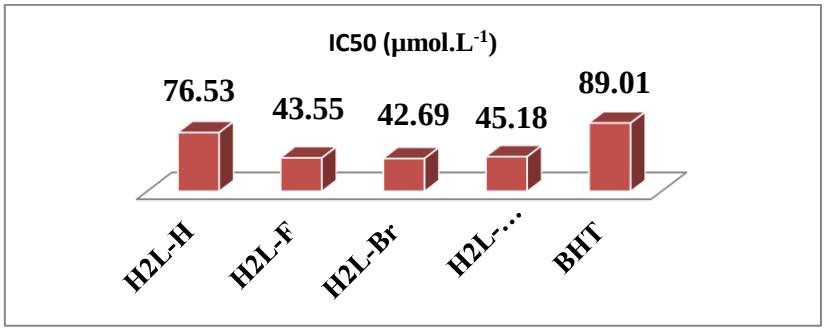

Figure 3. IC_{50} values representing $O_2^{\bullet-}$ radical scavenging for the compounds H_2L-Br, H_2L-F, H_2L-H, H_2L-NO_2 and the BHT standard

From **Figure 3**, it can be seen that compounds H_2L-NO_2, H_2L-Br and H_2L-F present the lowest values for IC_{50} in the order of 43.80±1.26 µmol. L^{-1} revealing the effect of electron-withdrawing groups (Bromo, Fluro and nitro) to increase the antioxidant activity, the lowest activity is represented by the compound H_2L-H with an IC_{50} of the order of 76.53 µmol. L^{-1}. The present results are in good agreement with the results of the antioxidant activity evaluated by the three chemical techniques published previously [9], this confirms the valuable role of the electron withdrawing groups in the increase the antioxidant activity [17]. According to the histogram illustrated in **Figure 3**, we can classify the tested compounds by order of their decreasing reactivity:

H_2L-Br > H_2L-F > H_2L-NO_2 > H_2L-H > BHT

3.3. Thermodynamic parameters

The study of the interaction of the four quinoline compounds with superoxide anion was estimated in terms of binding constant ($\boldsymbol{k_b}$), ratio of binding constants and standard Gibbs free energy ($\Delta G°$) (**Table 2**).
The k_b values are determined from the curves of the variation of log (1/C) versus log (i/i_0-i) plotted using the following equation [18]:

$$log\frac{1}{C} = logkb + log\frac{i}{i_0 - i} \quad (2)$$

Where C is the concentration of the tested compound (mol.L^{-1}), k_b is the binding constant (L.mol^{-1}), i and i_0 are the anodic current density in presence and absence of the tested compound, respectively.

Table 2. Values of $\boldsymbol{k_b}$ and $\Delta G°$ of the molecules H_2L-Br, H_2L-F, H_2L-NO_2, H_2L-H and the BHT standard.

Compound	Equation	R^2	k_b (L.mol^{-1})	ΔG°(kJ/mol)
$O_2^{\cdot-}$-H_2L-NO_2	y = 0.795x+4.418	0.996	26181.83	-26.21
$O_2^{\cdot-}$-H_2L-H	y = 0.396x+4.202	0.998	15922.08	-24.93
$O_2^{\cdot-}$-H_2L-F	y = 0.591x+4.345	0.986	22134.94	-25.78
$O_2^{\cdot-}$-H_2L-Br	y = 1.402x+4.408	0.970	25585.85	-26.15
$O_2^{\cdot-}$-BHT	y = 0.369x+4.22	0.979	16595.86	-25.04

From **Table 2**, we can notice that the derivatives H_2L-Br, H_2L-F and H_2L-NO_2 present the highest values of $\boldsymbol{k_b}$ constants compared to the derivative H_2L-H and the standard BHT confirming their strong interactions with the superoxide radical. The negative values of the free energies $\Delta G°$ indicate the spontaneity of the antiradical reaction which is considered as clear evidence of the efficiency of the tested compounds.

The ratio of the equilibrium binding constants (K_{Red}/K_{Ox}) was determined from the shift of the value of the formal potential using the following equation [19]:

$$\Delta E^0 = E_b^0 - E_f^0 = 0{,}059\ log\frac{K_{red}}{K_{ox}} \quad (3)$$

Where E_b^0 and E_f^0 are the formal potentials of the $\boldsymbol{O_2/O_2^{\cdot-}}$ redox couple in the bound and free forms. The values of the peak potential shift as well as the K_{red}/K_{ox} values for all the investigated compounds are summarized in **Table 3**.

The K_{Red}/K_{Ox} ratio values for compounds H_2L-H, H_2L-Br, H_2L-F and H_2L-NO_2 came out to be 1.42, 1.59, 1.21 and 1.53 respectively, which indicates that the interaction of the reduced form $\boldsymbol{O_2^{\cdot -}}$ with all derivatives is stronger than that of the oxidized form $\boldsymbol{O_2}$.

Table 3. Electrochemical data of $\boldsymbol{O_2^{\cdot -}}$ bound form of H_2L-Br, H_2L-F, H_2L-NO_2 and H_2L-H.

Compound	EP_a(V)	EP_c((V)	E^0(V)	ΔE^0(mV)	Kr/Ko
$\boldsymbol{O_2^{\cdot -}}$	-0.587	-1.133	-0.86	-	
H_2L-H - $\boldsymbol{O_2^{\cdot -}}$	-0.573	-1.129	-0.851	9	1.42
$\boldsymbol{O_2^{\cdot -}}$	-0.678	-1.02	-0.849	-	
H_2L-Br - $\boldsymbol{O_2^{\cdot -}}$	-0.691	-1.032	-0.861	1.2	1.59
$\boldsymbol{O_2^{\cdot -}}$	-0.589	-1.175	-0.882	-	
H_2L-F - $\boldsymbol{O_2^{\cdot -}}$	-0.586	-1.189	-0.887	5	1.21
$\boldsymbol{O_2^{\cdot -}}$	-0.673	-1.066	-0.869	-	
H_2L-NO_2 - $\boldsymbol{O_2^{\cdot -}}$	-0.632	-1.084	-0.858	1.1	1.53

$\boldsymbol{EP_c}$*:* cathodic potential; $\boldsymbol{EP_a}$*:* anodic potential; $\boldsymbol{E^0}=\frac{EPa+EPc}{2}$; $\boldsymbol{\Delta E^0} = E^0$ (H_2L-R- $\boldsymbol{O_2^{\cdot -}}$)-$E^0$ (H_2L-R).

4. Conclusion

By using the electrochemically generated $\boldsymbol{O_2^{\cdot -}}$ in situ, the reactivities of the four quinoline compounds was evaluated by cyclic voltammetry method. All derivatives reacted similarly with $\boldsymbol{O_2^{\cdot -}}$, inducing decrease in anodic peak current. The magnitude of calculated free energy displayed the strong interaction between the $\boldsymbol{O_2^{\cdot -}}$ and the investigated compounds. The negative values of ΔG° suggested the spontaneity of the electrostatic interaction of $\boldsymbol{O_2^{\cdot -}}$ with H_2L-H, H_2L-Br, H_2L-F, H_2L-NO_2 compounds.

Acknowledgement

We gratefully acknowledge Dr. Fatima Douadi from the University of Bourdj Bouariridj for the linguistic review of the manuscript.

References

[1] Y.F. Baba, N.K. Sebbar, S. Hayani, F.O. Chahdi, E.M. Essassi, Moroc. J. Hetero. Chem. **17** (2018) 83-126.
[2] H. Breuer, Atlas de la chimie, (2000).
[3] A. Korolkovas, Essentials of medicinal chemistry, John Wiley & Sons, (2008).
[4] J.J. Pocidalo, F. Vachon, B. Regnier, Les nouvelles quinolones, Arnette, (1985).
[5] J.C. Bergh, T.H. Tötterman, B.C. Termander, K.A.-M. Strandgarden, P.O.G. Gunnarsson, B.I. Nilsson, Cancer Investig. **15** (1997) 204–211.
[6] Y.F. Baba, H. Elmsellem, Y.K. Rodi, H. Steli, F.O. Chahdi, Y. Ouzidan, N.K. Sebbar, E.M. Essassi, F. El-Hajjaji, B. Hammouti, J. Mater. Environ. Sci. **7 (7)** (2016) 2424-2434
[7] I. Benmahammed, T. Douadi, S. Issaadi, M. Al-Noaimi, S. Chafaa, J. Disp. Sci. Tech. **41** (2019) 1002-1021.
[8] K. Douadi, S. Chafaa, T. Douadi, M. Al-Noaimi, I. Kaabi, J. Mol. Struct. **1217** (2020) 128305.
[9] M.M. Kornet, O.A. Brazhko, M.P. Zavhorodniy, V.V. Tkach, O.S. Kruglyak, Y.G. Ivanushko, S.C. de Oliveira, P.I. Yagodynets, bio inter. Res. App. Chem. **11** (2021) 9148 - 9156.
[10] I. Bazine, Z. Cheraiet, R. Bensegueni, C. Bensouici, A. Boukhari, J. Hetero. Chem. **57** (2020) 2139–2149.
[11] A.A. Nagargoje, S.V. Akolkar, M.M. Siddiqui, D.D. Subhedar, J.N. Sangshetti, V.M. Khedkar, B.B. Shingate, Chem. Biodiver. **17** (2020) e1900624.
[12] M. Al-Noaimi, O.S. Abdel-Rahman, I.I. Fasfous, M. El-Khateeb, F.F. Awwadi, I. Warad, Spectrochim. Acta Part A: Mol. Biomol. Spect.**125** (2014) 375–383.
[13] T. Lanez, H. Hemmami, Current Pharm. Anal. **13** (2017) 110–116.
[14] N. Blanc, D. Hauchard, L. Audibert, E.A. Gall, Talanta. **84** (2011) 513–518.
[15] T. Lanez, M. Henni, J. Iran. Chem. Soc. **13** (2016) 1741–1748.
[16] C. Le Bourvellec, D. Hauchard, A. Darchen, J.-L. Burgot, M.-L. Abasq, Talanta. **75** (2008) 1098–1103.
[17] F.C. Torres, N. Brucker, S. Fernandes Andrade, D. Fabio Kawano, S. Cristina Garcia, G. Lino von Poser, V. Lucia Eifler-Lima, Cur. Top. Med. Chem. **14** (2014) 2600–2623.
[18] G.-C. Zhao, J.-J. Zhu, J.-J. Zhang, H.-Y. Chen, Anal. Chim. Acta **394** (1999) 337–344.
[19] X. Chu, G.-L. Shen, J.-H. Jiang, T.-F. Kang, B. Xiong, R.-Q. Yu, Anal. Chim. Acta **373** (1998) 29–38.

Journal of Physical & Chemical Research

Journal homepage:

Electrochemical behavior of dibutyl methyl ester p-tert-butyl calix [4] arene

Lilia Tabti[1], Mohamed redha Khelladi [1, 2*], Embarek Bentouhami[1,3]

[1]LCIMN, Laboratory, University Ferhat Abbas Setif-1, 19000 Sétif, Algeria
[2]Department of Materials Science, Faculty of Sciences and Technology, Mohamed El Bachir El Ibrahimi University, Bordj Bou Arreridj 34030, Algeria
[3]Department of Process Engineering, Faculty of Technology, University Ferhat Abbas Setif-1, 19000 Sétif, Algeria

** Corresponding author: Tel./Fax: +213-0794 62 6143; E-mail address: mohamedridha.khelladi@univ-bba.dz*

Article history
Received March 20, 2022
Accepted for publication April 10, 2022

Abstract

The electrochemical behavior of dibutyl methyl ester *p*-tert-butyl calix [4] arene compound 1 was studied by cyclic voltammetry. At 25˚C and scan rate of 20 mVs^{-1}. The anodic peak is affected by scan rate, concentration and temperature is a totally irreversible process**.** The result shows that there is an irreversible electrochemical oxidative wave when the potential is more 1.3 V versus Ag/AgCl in an acetonitrile.

Keywords: Calix[4]arene, Electrochemistry, Cyclic voltammetry, platinum electrode, Diffusion coefficient

1. Introduction

The name calixarenes was introduced by Gutsche [1] for the cyclic oligomers ,the use of this word (calix means beaker in Latin and Greek) was suggested in particular by the shape (cup) of tetramer with upper and lower rims and central annulus [2, 3] which are a well-established class of compound in today's in supramolecular chemistry. p tert butyl calix[*n*]arenes (*n* = 4, 6, 8) can be easily obtained by the condensation of P-substituted phenol and formaldehyde [4.5], can be converted into various derivatives by chemical modifications. Obvious places to

introduce additional functionalities are the phenolic oxygen, which can be converted to ether or ester groups and the p-positions. Which are available for all types of electrophilic substitutions after removal of the t-butyl groups.[6, 7] Calixarenes and their derivatives have attracted much attention over the past decade as the basis for molecular and ionic recognition because of their conformational and structural flexibility makes them highly attractive platforms for the synthesis of more evolved macro cyclic receptors [8-10] which can be used as ion sensitive electrodes or sensors, optical sensors, chiral recognition devices for solid phase extraction, as a stationary phase and modifiers [11-13].

Scientists always pay attentions to the electrochemical properties of water-soluble calixarenes. For example, Paillert and Diao [9, 10] reported the electrochemical characteristics of p-sulfonated calix [6]arene. Guowang Diao and Jing Gu reported the electrochemical properties of p-sulfonated calix [4]arene [14] and p-sulfonated calix[6]arene [10]. The results showed that both p-sulfonated calix[6]arene and p-sulfonated calix[4]arene could be oxidized and their anodic waves occurred due to the oxidation of phenolic group. Nevertheless, A few articles reported the electrochemical properties of p-tert-butyl calixarenes in organic solvent. Pailleret and al. [15] studied the electrochemical behaviors of both p-tert-butyl calix [4]arene and p-tertbutyl calix[6]arene in dichloromethane . Pailleret and Arrigan. [13] reported the electrochemical oxidation of tetra ester calix [4]arene in acetonitrile In this article, we are interested in examining the electrochemical behavior of dibutyl methyl ester *p*-tert-butyl calyx [4] arene . The results show there is two peak anodic waves when the potential ranges from -0.1 to 2.0 V versus Ag/AgCl, due to the oxidation of the dibutyl methyl ester *p*-tert-butyl calix [4] arene.

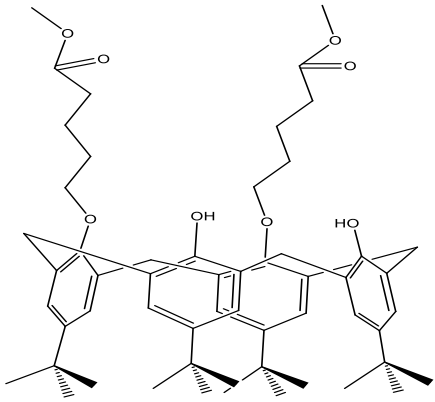

Scheme 1. Chemical structure of compound 1.

2. Experimental

Compound 1, dibutyl methyl ester *p*-tert-butyl calix [4]arene . Was prepared according to literature methods [16, 17] Solutions of this compound are prepared in acetonitrile with the background electrolyte tetrabutyl ammonium perchlorate (0.1 M). This was synthesized according to House et al. [18]. The electrolyte solution was deoxidized by bubbling with nitrogen for 10 min prior to performing the electrochemical measurements. The conventional electrochemical measurements were taken using a glass cell consisting of a three-electrodes assembly that was connected to a VoltaLab 40 (PGZ301 & Volta Master 4) controlled by a personal computer. The counter electrode was a platinum wire (10 mm) the working electrode was a platinum disk (2 mm) and the reference electrode was (Ag/AgCl, 8 mm) in organic phase. The working electrode was rinsed in water, then acetonitrile and allowed to dray in air before use.

3. Results and Discussion

The electrochemical behaviors of compound **1** on Ag/Ag^{+} were investigated by cyclic voltammetry. At scan rate of 20 mVs^{-1} and 25°C, the cyclic voltammogram of compound **1** is 5×10^{-4}M + 0.1M TBAP in acetonitrile is shown in Figure 1 (the solid line red). The background (the solid line black) is also shown in Figure 1. No electrochemical reaction occurs in the blank buffer solution containing compound **1** in our experimental potential window. It is clear that there is two anodic waves observed when the potential is scanned from -0.1 to 2.0 V versus Ag/Ag^{+}, the first peak potential is 1.48 V. Compared with p-tert-butyl calix [8]arene and phenolic calixarenes The first conclusion to draw from these observations is that the phenol moieties of parent calixarenes are electrochemically active in organic media, as expected from the known electroactivity of phenols [16, 19]. The second peak potential observed is 1.80V, due to the oxidation of the hydroxyl group [20].

The voltammograms of compound 1 recorded in multi-cycles are shown in Figure 2 at a scan rate of 20 m Vs^{-1}. Repetitive potential cycling do not show any substantial alteration of the initial intense and irreversible oxidation peak upon repeated potential cycling this indicates that electrochemical oxidation of compound 1 are oxidisable but did not passivate the electrode surface [20].

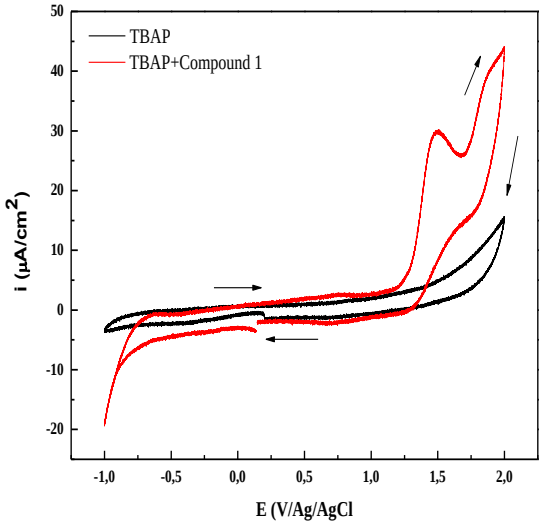

Figure 1. The voltammograms of the background and the solution containing 5 × 10^{-4} M compound 1 + 0.1M TBAP in acetonitrile at scan rate of 20 mVs^{-1} and 25 ◦C.

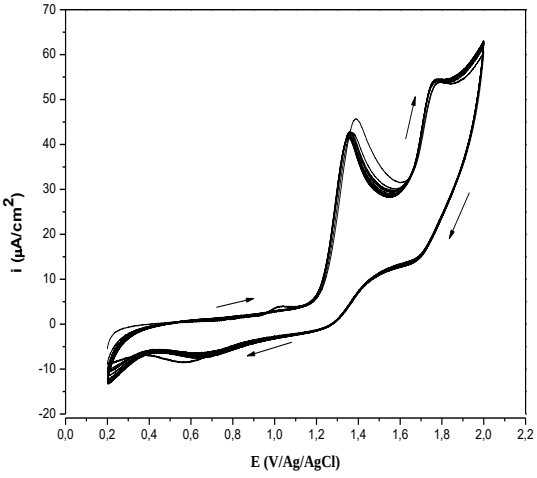

Figure 2. The voltammograms for multi-cycles of 5 × 10^{-4} M compound 1 in acetonitrile at scan rate of 20 mVs^{-1} and 25 ◦C.

3.1 Measurements of n, D_R, and α

At 25 ˚C , As shown in **Figure 3**, both anodic peak potential, E_p and peak current, i_p are affected by the scan rate, v. According to Nicholson [21], for an irreversible anodic reaction, the relationship between E_p and ln v is linear, and can be described as follows:

$$E_P = E^\circ + \frac{RT}{\alpha n_a F} + \left[0.780 + \ln\left(\frac{D_R}{K^\circ}\right)^{\frac{1}{2}} + \left(\frac{\alpha n a F}{RT}\right)^{\frac{1}{2}}\right] \quad (1)$$

where E° is the formal standard potential, R the gas constant, n_a the number of the electrons transferred in the rate determining step , a the electron transfer coefficient, F the Faraday constant, T the absolute temperature. D_R diffusion coefficient of compound 1, T the absolute temperature, and K° the standard heterogeneous reaction rate constant.

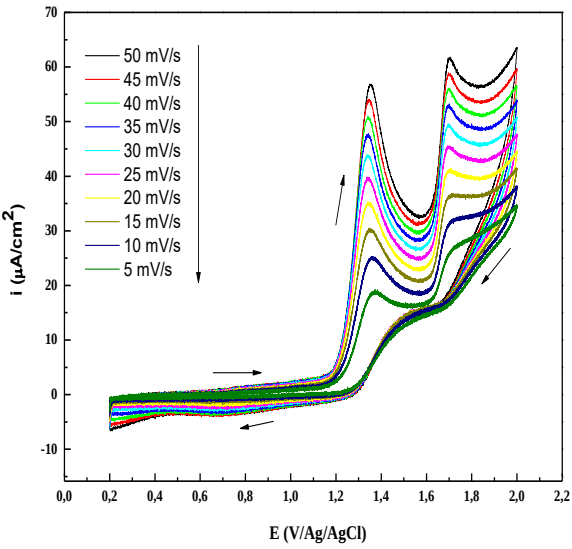

Figure 3. The voltammograms of 5× 10^{-4} M compound 1 + 0.1M TBAP in acetonitrile at different scan rates with 25°C.

According to the slope of the straight line of E_p against log *v*, is shown in Figure 4. The product of α and n_a can be evaluated as 1.29.

The peak current i_P for an irreversible electrochemical reaction can be described as follows [21]

$$i_p = (2.99 \times 10^{-5}) n (\alpha n_a)^{\frac{1}{2}} \times A C_R {D_R}^{1/2} V^{1/2} \quad (2)$$

Where n represents the number of electrons transferred in the electrochemical reaction, A the area of the electrode, C_R the initial concentration of compound 1.

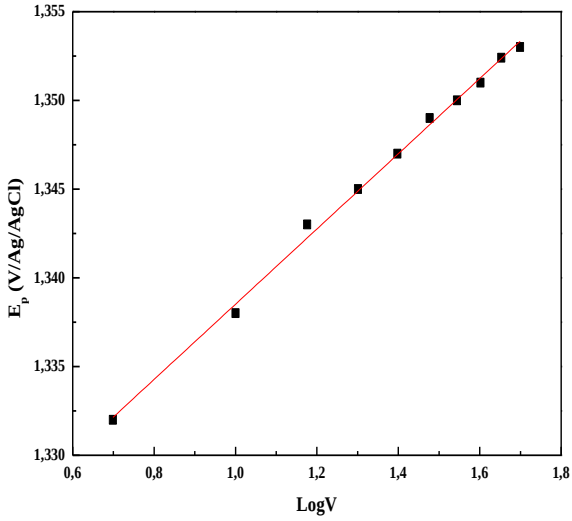

Figure 4. The plot of the anodic peak potential and the natural logarithm of the scan rate. The experimental conditions are the same as these described in figure 3.

According to Eq. (2), at a given initial concentration of III, the plot of i_p versus $V^{1/2}$ must be straight line. Figure 5 shows the experimental results. From the slope of the straight line, can be evaluated the value of $\left(n(\alpha n_a)^{\frac{1}{2}} \times {D_R}^{1/2}\right)$ in 1.7×10^{-3}cm $s^{-1/2}$

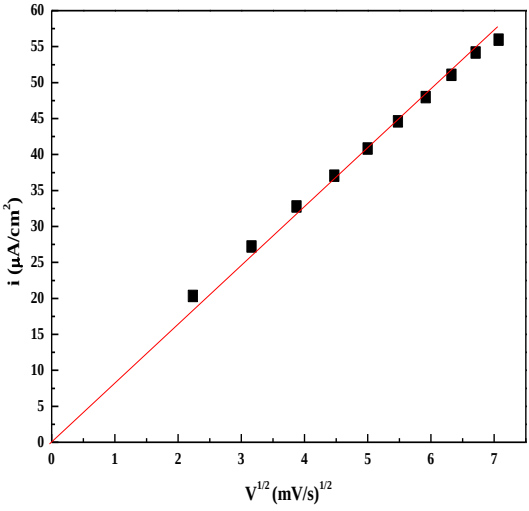

Figure.5. The relationship between the peak current Ip and the square root of scan rate $V^{1/2}$. The experimental conditions are the same as these described in figure 3.

Figure 6. presented the voltammograms at different concentrations of compound 1. The value of of $\left(n(\alpha n_a)^{\frac{1}{2}} \times {D_R}^{1/2}\right)$ can also be obtained by plotting i_p versus the concentration, C_R of compound 1 according to a scanning rate, at 20 m Vs^{-1} the straight lines between i_p and C_R are plotted and are shown in Figure 7. According to the slopes of these lines, can be calculated the values of $\left(n(\alpha n_a)^{\frac{1}{2}} \times {D_R}^{1/2}\right)$ as 1.6×10^{-3}cm $s^{-1/2}$.

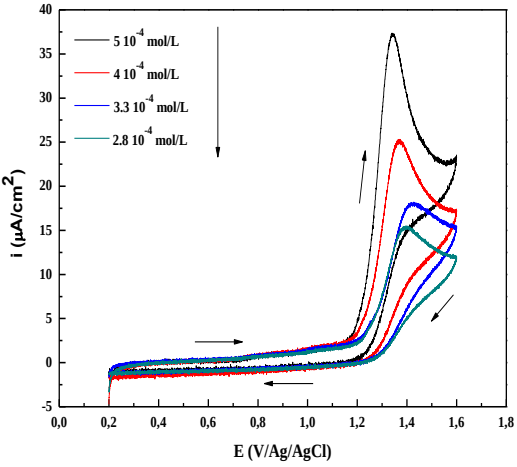

Figure 6. The votammograms of compound 1 at different concentration, 25°C and 20 mVs^{-1}.

The error for both results calculated is located within the mistake of our experiments bar. The mean value is 1.65×10^{-3}cm $s^{-1/2}$**,** that is the same as that measured by plotting i_p versus$V^{1/2}$. As described formerly, the value of $\alpha n_a$is 1.29. Combination of two settings αn_a and $\left(n(\alpha n_a)^{\frac{1}{2}} \times {D_R}^{1/2}\right)$ we can obtain the value of the product of n and ${D_R}^{1/2}$ the value of ${nD_R}^{1/2}$ is calculated as 1.47×10^{-3}cm $s^{-1/2}$.

For determining the value of n and D_R, a steady state voltammogram was measured by a platinum disc microelectrode (diameter: 2 mm). Was determined and represented in Figure 8.The limited current diffusion, it is measured as 0.51µA. The value of of nD_R is calculated as 0.2 cm^2 s^{-1} by using the relationship $i_l = 4nFD_RC_R$ [20], the diffusion coefficient, D_R of compound 1 may be evaluated as 6.5×10^{-5} cm^2s^{-1}, and *n*, the number of electrons transferred in the electrochemical oxidation of compound 1, *n* is taken as 2, which is greater than that of *p*-sulfonated sodium salt of calix [6] arene in solution studied [10]. The result shows that it is advantage for the electrochemical oxidation of calixarene in organic solvent.

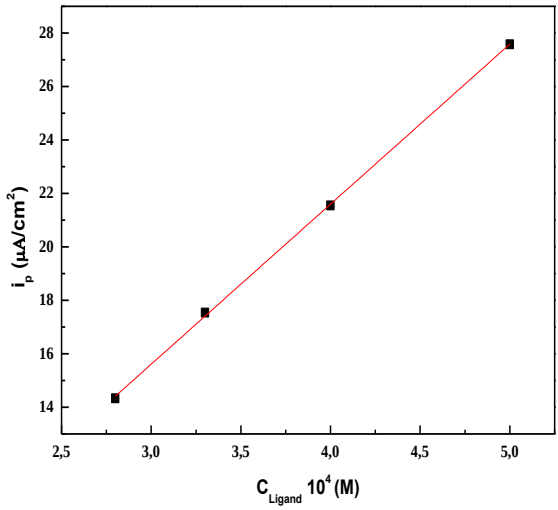

Figure 7. At 25°C, the relationships between I_p and the concentration of compound 1.

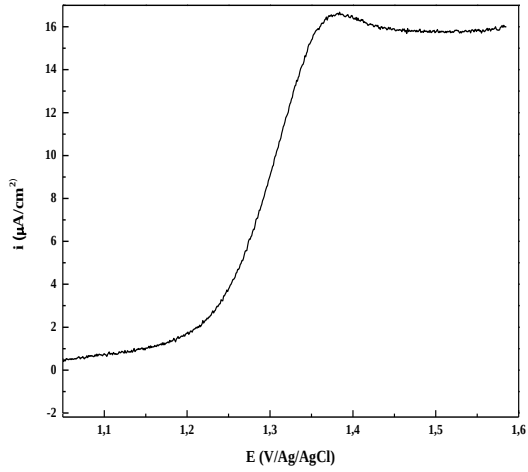

Figure 8. The steady state voltammograms of compound 1 on an platinum disc electrode with scan rate of 5 mVs^{-1}. The other experimental conditions are the same as those described in figure 3.

3.2 Temperature dependence

At different temperature, the voltammograms of compound 1 are presented in Figure 9. The anodic peak current increased with the temperature. At higher temperature, the peak potential shifts in the negative direction, this means that it is easier for the oxidation of compound 1 [14, 19].

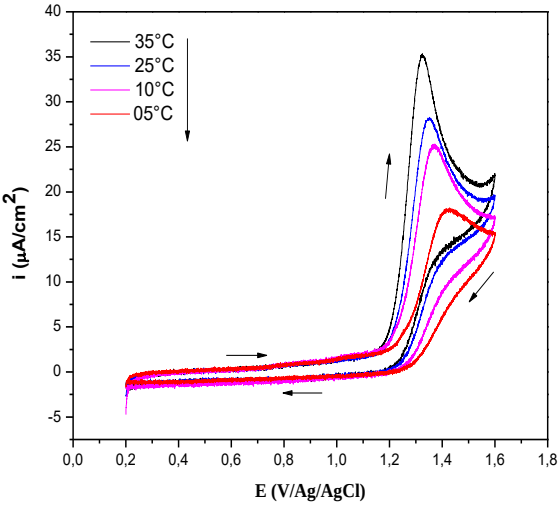

Figure 9. The voltammograms of compound 1 on platinum disc electrode with scan rate of 5 mVs^{-1}at different temperature.

4. Conclusion

In acetonitrile, compound 1 can be oxidized on platinum electrodes. The anodic peak potential is observed as 1.48 and 1.74 V (versus Ag/AgCl) at 25° C**.** The result shows that there is an irreversible electrochemical oxidative wave. The number of the electrons transferred in the electrochemical reaction is 2. The diffusion coefficient of compound 1 is $6.5\times10^{-5}\ cm^2s^{-1}$.

References

[1] C.D. Gutsche, *Calixarenes Revisited*, Royal Society of Chemistry: Cambridge (1998).
[2] V. Bohmer. Chem. Int. Ed **34** (1995) 713-745.
[3] S. Bouhroum. J.S. Kim, S.W. Lee, P. Thuéry, G. Yal, F. Arnoud-Neu, J. Vicens, J. Incl. Phenomen. Macrocycl. Chem **62** (2008) 239-250.
[4] B.S. Creaven, D.F. Donlon, J. Moginley, Coord. Chem. Revi **253** (2009) 893-962.
[5] J. Schatz, F. Schildbach, A. Lentz, S. Rastatter, J. Chem. Soc. Perkin Trans **2** (1998) 75-78.

[6] G. Gormar, K. Selffarth, M .Schulz, J. Zimmermann, G. Flamig, Die Makromol. Chem **191**(1990) 81-87.
[7] C. Gruttner, V. Bohmer, Teterahedron Letters **35** (1994) 6267-6270.
[8] Y. Wu, S. Zhai, L. Qiang, L. Gao, F. Wang, J. Chin. Chem. Soc **62** (2015) 342-348.
[9] A. Pailleret, N. Magan-Oliva, S. Ollivier, D.N.M. Arrigan. J. Electroanal. Chem **508** (2001) 81-88.
[10] G. Diao, Y. Liu, Electroanalysis **17** (2005) 1279-1284.
[11] V.V, Egorov, Y.V. Sinkevich, Talanta **48** (1999) 23-28.
[12] C. Lynam, K. Jennings, D. Diamond, Anal. Chem **74** (2002) 59-66.
[13] Mc.G. Mohan, S.O. Malley, K. Nolan, D. Dianond, Arkivoc **7** (2003) 23-31.
[14] G. Diao, W. Zhou, J. Electroanal. Chem **15** (2004) 325-330.
[15] A. Pailleret, G. Herzog, D.W.M. Arrigan,. Electrochem.Com **5** (2003) 68-72.
[16] M.A. Mckervey, E.M. Seward, G. Ferguson, B. Rull, S.J. Harris, J. Chem. Soc. Chem. Commun (1985) 388-390.
[17] F. Arnaud-Neu, E.M. Collins, J. Am. Chem. Soc **111** (1989) 8681-8691.
[18] H.O. House, E. Feng, N.P. Peet, J. Org. Chem **36** (1971) 2371-2375.
[19] G. Diao, J. Gu, J. Electrochim. Acta **52** (2006) 42-46.
[20] R. Vataj, A. Louati, C. Jeunesse, D. Matt J. Electroanl. Chem **565** (2004) 295-299.
[21] A. J. Bard, L. R. Faulkner, Electrochemical Methods-Fundamentals and applications, 2nd Ed., Wiley, New York (2001).

Journal of Physical & Chemical Research

Journal homepage:

Potentiostatic electrosynthesis of polypyrrole film onto silicon support

Imene Chikouche[*1,2] and Charif Dehchar[1,3]

[1] *Laboratoire Croissance et Caractérisation de Nouveaux Semi-conducteurs, Faculté de Technologie, Université Sétif 1, Algérie.*
[2] *Département des Sciences de la matière, Faculté de Technologie, Université de Bordj Bou Arréridj, Algérie.*
[3] *Département de Génie des procédés, Faculté de Technologie, Université 20 août 1955, Skikda, Algérie.*

* Corresponding author: E-mail address: chikouche_imene@yahoo.fr

Article history
Received March 29, 2022
Accepted for publication April 13, 2022

Abstract

This work reports the electrochemical synthesis of polypyrrole (PPy) films onto silicon (Si) support in an organic solution using potentiostatic mode of electrodeposition. Electrodeposition of PPy was conducted under oxidative conditions; the current transient curve, taken at constant potential of 1.1 V, was discussed. The microstructure of the polypyrrole (PPy) films obtained is examined by SEM and AFM.

Keywords: oxidation, polymerization, potential, pyrrole.

1. Introduction

Conductive organic polymers, due to their structure, electrical conductivity and specific surface area of the polymer film, constitute a family of materials required in many application areas. They act as supports for the various metals to form composite films, thus acquiring high electrocatalytic properties which make these materials an alternative of choice for many applications where the use of catalysts in the metallic state is limited by their high cost, such as fuel cells and biofuel cells.

These polymers can be synthesized by oxidative polymerization either chemically or electrochemically. Of the organic monomers leading to electronically conductive polymers, pyrrole (Py) is the easiest to oxidize

[1-3]. It was first synthesized in 1916 by Angeli and his group. The synthesis was carried out by chemical oxidation of pyrrole in the presence of H_2O_2 and the resulting product, called "Black Pyrrole", was in the form of an amorphous powder. However, in order to better control the structure of the polymer, and thus its properties, electrochemical polymerization, commonly known as "electropolymerization", is the most appropriate synthesis method. It should also be noted that among the parameters influencing electropolymerization, the applied potential can play a determining role in the quality of the polymer formed in terms of density, continuity, adhesion and microstructure of the deposit [4- 5].

Hereine, we report the synthesis of polypyrrole on silicon supports via electrochemical method under potentiostatic deposition mode. The evolution of current transient as a function of time at constant applied potential are discussed and the microstructure of the as-formed PPy films are examined by microscopy via SEM and AFM techniques.

2. Experimental

Electrochemical experiments were conducted in a conventional three-electrode cell at room temperature. Platinum (Pt) wire and saturated calomel electrode (SCE) $Hg/Hg_2Cl_2/KCl$ (3M) were used as the counter and reference electrode, respectively.

Polymerization of pyrrole was accomplished under galvanostatic control on n-doped silicon (Si) wafer from an organic solution of 5 mM pyrrole and 0.1 M lithium perchlorate ($LiClO_4$) dissolved in acetonitrile (CH_3CN). During preparation of the electrode, the projected surface area of the Si substrate was 0.4 cm^2.

3. Results and discussion

3.1. Study of the polypyrrole stability on silicon support

In order to verify the stability of the PPy film obtained on a new material (silicon), we studied by cyclic voltammetry the electrochemical behavior of our monomer in an organic medium on a silicon electrode. As the electropolymerization of the monomer is carried out by anodic oxidation, the field of study chosen is located in the anodic zone. Figure 1 shows the voltammogram for a 10^{-1} M CH_3CN/ $LiClO_4$ solution containing 5 mM of pyrrole, recorded at a scan rate of 50 mV/s.

During the first scan, a very intense peak is observed around 1 V/SCE, corresponding to the oxidation of the monomer (Py) into its cation radical which leads to the formation of the dimer adsorbed on the surface of the electrode. During the return scan, there is a characteristic crossing of the nucleation-growth phenomena of the polypyrrole.

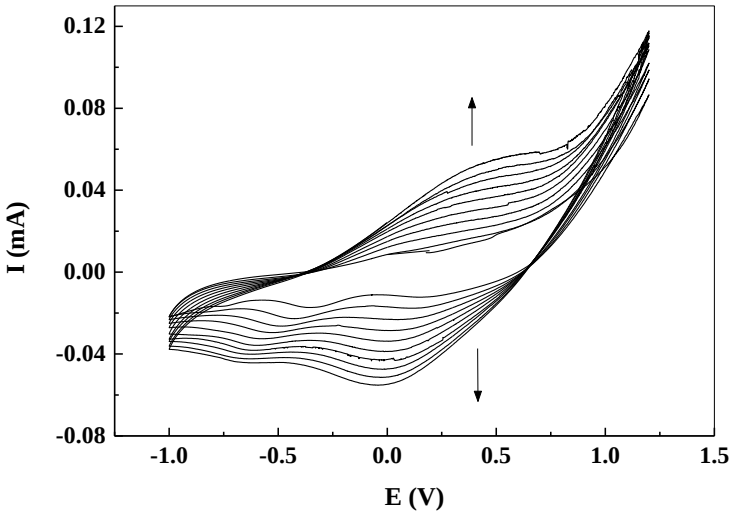

Figure 1. Cyclic voltammetry of pyrrole electropolymerization on silicon in 0.1M CH_3CN/ $LiClO_4$ containing 5 mM of pyrrole. Scan rate = 50 mV/s

We also note an increase in the current intensity of the oxidation and reduction peaks. This increase in oxidation and reduction currents is explained by the growth of the PPy film on the silicon electrode surface.

After having synthesized the polypyrrole film on silicon, we proceeded to study the PPy electroactivity by cyclic voltammetry, in a monomer-free solution (0.1 M KCl). Figure 2 presents the voltammogram obtained at a scanning speed equal to 20 mV/s.

The presence of large anodic and cathodic waves shows that the deposits are electroactive, stable and exhibit good redox behavior. The redox property of polypyrrole is related to the processes of insertion/expulsion of anions and cations. The ion present in the supporting electrolyte easily diffuses inside and outside the polymer during redox processes to neutralize the charge of the polypyrrole film.

We also note that the positions of oxidation and reduction peaks are different. The potential difference $\Delta E = |E_{pc} - E_{pa}|$ is not zero, which shows that the polymeric film PPy has good reversibility.

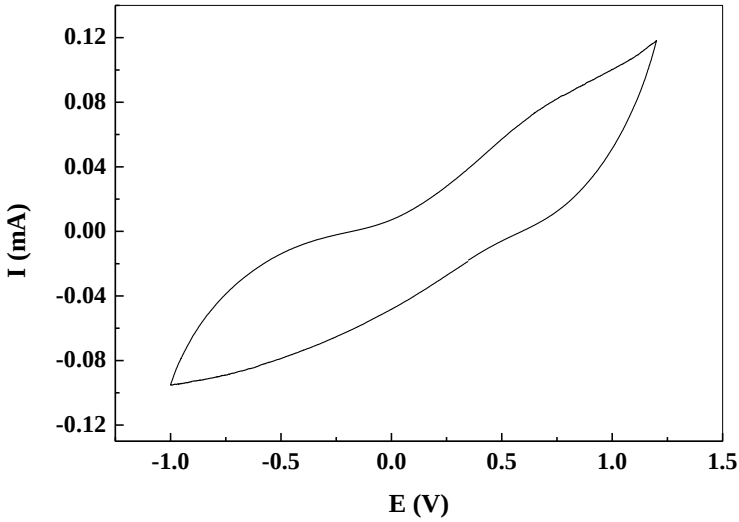

Figure 2. Electroactivity test of the deposited PPy film in a pyrrole-free solution.

3.2. Polymerization of pyrrole by chronoamperometry

In this section, we will study the formation of polypyrrole deposits by imposing a potential between the working electrode and the reference electrode.

The deposition potential that we have chosen from the cyclic voltammogram of figure 1 is 1.1 V, this potential allows continuous oxidation of the monomer on silicon.

We report in figure 3 the current evolution as a function of time recorded during the electrodeposition of PPy on silicon in potentiostatic mode. On the curve obtained, three main zones can be distinguished: after the double layer has been charged, the current density increases very rapidly and reaches a maximum value i_{max} after a very short time ($t < 1$ s), this is attributed to the growth of a new phase and the increase in the number of nuclei formed on the electrode surface. Then, the current density gradually decreases with time to a steady state where it remains unchanged.

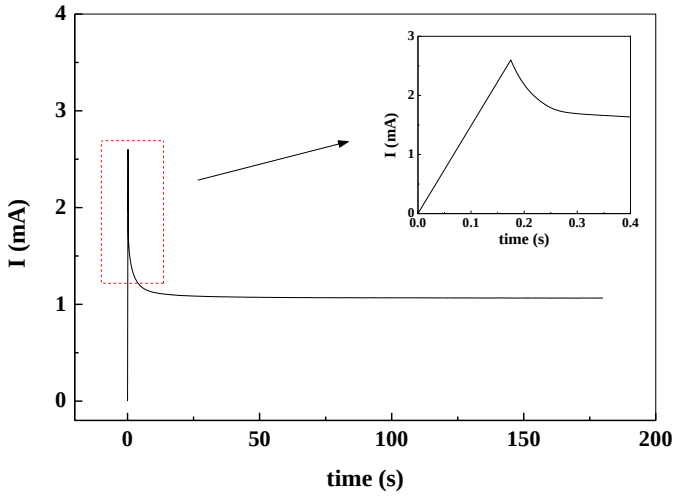

Figure 3. Current transient curve of PPy on Si. E = 1.1 V.

3.3. Electrosynthesis of PPy at different applied potentials

When potentiostatically depositing PPy, it is very important to carefully choose the applied potential, as this determines the amount of polymer that will be deposited, and then it determines the final characteristics of the polymer layer. In our study, we tested the effect of this crucial factor by imposing different constant potentials, from 0.9 to 1.2 V, and we followed the evolution of the current versus time. The curves obtained are shown in figure 4.

It can be seen that the curves obtained all have the same appearance. It is also observed that as the imposed potential increases, the current density i_{max} increases, which influences the quantity of polymer deposited on the electrode surface.

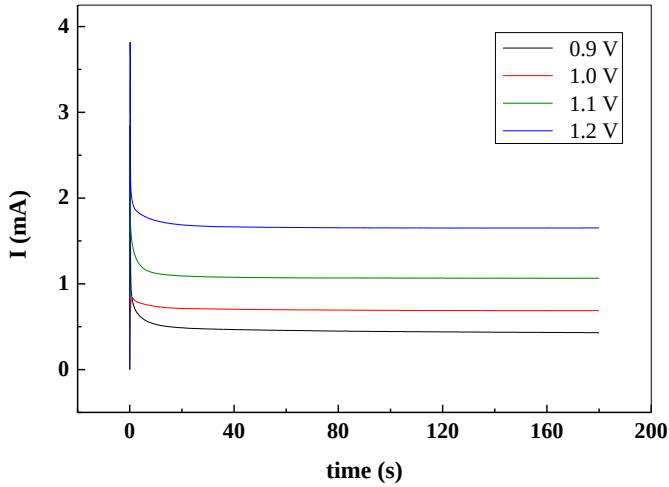

Figure 4. Electropolymerization of pyrrole on silicon electrode by the potentiostatic method at different imposed potentials.

3.4.Characterization of the PPy films obtained

The morphological characteristics of the obtained PPy film were examined by the atomic force microscope (AFM) and by scanning electron microscopy (SEM). As shown in Figure 5, the PPy layer covers the entire silicon surface. It has a relatively rough surface (RMS=108.263 nm).

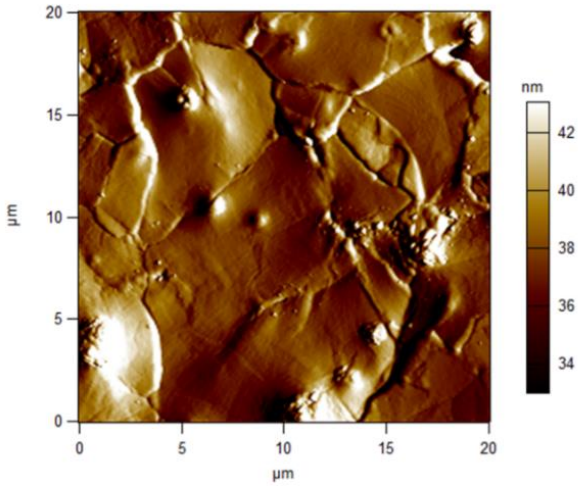

Figure 5. 2D AFM image of PPy film prepared at 1.1V.

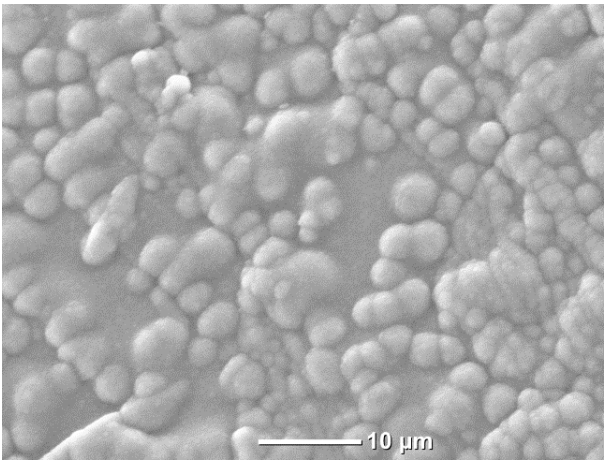

Figure 6. SEM image of the PPy film deposited on silicon at 1.1V.

The SEM micrograph of the polypyrrole film deposited on silicon using the potentiostatic mode (Figure 6) shows a homogeneous surface morphology characterized by a globular structure formed by homogeneous globules distributed over the entire surface of the deposit.

4. Conclusion

In this work, we electrochemically synthesized polypyrrole films onto silicon substrates by imposing an oxidation potential in an organic medium of pyrrole. Potentiostatic mode of electrodeposition leads to a well adhering homogeneous polypyrrole films on silicon supports. The structure of the as-formed film, as shown by SEM technique, represents a very promising support to receive a multitude of other phases, namely metallic particles, to prepare active materials.

References

[1] Hernandez, R. Diaz, A. F. Waltman, R. Bargon. J. Physical Chemistry **88** (1984) 3333.
[2] Adhikari, A. These of Pune University, Ind 2004.
[3] Armour, M. Davies, A. G. Upadhyay, J. Wasserma. A. J. Polymer Science Part a-1-Polymer Chemistry, **5** (1967) 1527.
[4] C. Dehchar, I. Chikouche, R. Kherrat, S. Zougar, A. Zouaoui, Surf. Rev. Lett. 24 (2017) 1750118.
[5] I. Chikouche, C. Dehchar, A. Sahari, N. Loucif. Surf. Rev. Lett. **5** (2019) 1850187.

Journal of Physical & Chemical Research

Journal homepage:

Elaboration et caractérisation des couches minces d'oxyde de cuivre : Application à la photo-dégradation de Méthyle Orange

Asma Azzoug[1,2], Imene Abid[1], Samiha Laidoudi[3], Ouafia Belguerbi[4,5], Ouidad Baka[1,6], Mohamed Redha Khelladi[1,2*]

[1]*Laboratoire de chimie ingénierie moléculaire et nanostructure (LCIMN), Université Ferhat Abbas Sétif-1, 19000, Algérie.*
[2]*Département Sciences de la Matière, Faculté Sciences et de la Technologie, Université Mohamed El Bachir El Ibrahimi Bordj Bou Arreridj 34000, Algérie.*
[3]*Département Sciences et techniques, Faculté Sciences et de la Technologie, Université Mohamed El Bachir El Ibrahimi Bordj Bou Arreridj 34000, Algérie.*
[4]*Research Center in Industrial Technologies CRTI, P.O.Box 64, 16014 Cheraga, Alger, Algérie.*
[5]*Laboratoire d'Energétique et Electrochimie du Solide, Département de Génie des Procédés, Faculté de Technologie, Université Ferhat Abbas Sétif-1, 19000 Sétif, Algérie.*
[6]Département de génie des procédés, Université Kasdi Merbah, 30000 Ouargla, Algérie
** Corresponding author: Tel./Fax: +213-0794 62 6143; E-mail address: mohamedridha.khelladi@univ-bba.dz*

Article history
Received April 02, 2022
Accepted for publication April 12, 2022

Abstract

Dans ce travail nous avons étudié l'effet du temps de déposition sur les différentes propriétés des couches minces d'oxyde de cuivre. En premier lieu nous avons élaboré des films minces de Cu_2O par électrodéposition sur un substrat ITO dans un milieu sulfate à température fixé de T=60° et un potentiel imposé de - 0.5V/ECS. En second lieu les couches minces de l'oxyde de cuivre (Cu_2O/ITO) ont subi un traitement thermique à température de 500 °C pendant 1h pour obtenir des films mince nommé CuO/ITO. Les couches minces déposées ont été caractérisées par la diffraction du rayon X (DRX), la microscopie à force atomique (AFM), le microscope électronique à balayage (MEB) et la spectroscopie UV-Vis. L'activité photocatalytique des films Cu_2O et CuO a été étudiée au moyen de la dégradation du méthyl orange (MO) sous irradiation directe de rayons UV. Les propriétés photocalytique montrent des meilleures vitesses de dégradation avec une constante de vitesse de l'ordre 0,00087 min^{-1} pour Cu_2O et 0.0025 min^{-1} pour CuO.

Keywords: Electrodéposition, Méthyle orange, Oxyde de cuivre; Photodégradation.

1. Introduction

Les oxydes conducteurs transparents (TCO) ont fait l'objet d'une attention considérable en raison de leur grande transparence optique dans le visible, et leur excellente conductivité électrique [1]. Ces oxydes ont suscité un intérêt considérable en raison de leurs applications potentielles telles que les cellules solaires, les capteurs, les supercapaciteurs, la photocatalyse, les dispositifs électro-chromes… [1-6]. Parmi eux, l'oxyde de cuivre avec ces deux formes à savoir: la ténorite (CuO) et la cuprite (Cu_2O) de bande interdite de 1.2-1.7 eV et 1.9-2.2 eV, respectivement. Ces oxydes ont suscités un grand intérêt auprès de la communauté scientifique à travers le monde entier [7, 8]. Ces deux oxydes ont un caractère semi-conducteur de type p due à la présence des lacunes de cuivre dans leurs structures cristallographiques, avec des avantages qui sont : faible coût, toxicité faible et une grande stabilité [1,2]. De nos jours, les méthodes utilisées pour déposer des couches minces d'oxyde de cuivre sont différents. Parmi ces méthodes, la déposition électrochimique ou l'électrodéposition, elle est couramment utilisée grâce à la facilité de sa manipulation, moins onéreuses et à la possibilité de faire varier les propriétés des structures en jouant sur les différents paramètres de déposition tels que les précurseurs, les concentrations, les additifs, le substrat, la température, le temps de déposition, le pH, le potentiel de déposition, etc.

Jusqu'à présent, les colorants organiques non biodégradables retirés de l'industrie mettent en danger la vie aquatique et perturbent l'environnement [9]. Par conséquent, plusieurs techniques ont été développées pour éliminer ces effluents, comme l'adsorption, la biodégradation et l'oxydation catalytique humide. Parmi celles-ci, la dégradation photocatalytique, qu'est une méthode économique et innovante pour éliminer complètement les polluants organiques [10,11]. Ceci est dû au fait que la dégradation photocatalytique des colorants organiques est une stratégie prometteuse pour résoudre la pollution de l'eau. Les avantages de la dégradation photocatalytique sont : le faible coût, la propreté et respect de l'environnement, qui peut être initiée en utilisant l'énergie solaire [12]. Habituellement, les réactions photocatalytiques se produisent à la surface des semi-conducteurs (oxyde métallique). En principe, l'irradiation d'un oxyde métallique induit le transfert d'électrons de la bande de valence à la bande de conduction, ce qui conduit à la dégradation des polluants [13].

Dans ce travail, nous avons élaboré des couches minces d'oxyde de cuivre (Cu_2O et CuO) par la méthode d'électrodéposition à différente temps de dépôts sur un substrat ITO. Les films préparés ont été caractérisés par différentes techniques de caractérisation telles que: diffraction des rayons X (DRX), microscopie à force atomique (AFM), microscopie électronique à balayage (MEB) et spectroscopie UV-Visible.

En final nous avons utilisé les couches de Cu_2O et CuO synthétisés dans la dégradation photocatalytique de méthyle orange (OM).

2. Méthodes Expérimentales

2.1 Dispositifs électrochimique

Les expériences électrochimiques ont été réalisées dans une cellule électrochimique à trois électrodes reliées et contrôlées par un Potentiostat/Galvanostat (voltalab PGZ 301) piloté par ordinateur à l'aide d'un logiciel Voltalab 4. Une électrode au calomel saturé (ECS) et une plaque de platine (Pt) ont été utilisés comme référence et contre-électrode, respectivement. Un substrat de verre recouvert d'une couche semi-conductrice d'étain dopé en indium (ITO) a été utilisé comme électrode de travail dont la résistivité est 8 à 12 Ω/cm^2. La surface de l'ITO immergé dans électrolyte est de 1 cm^2. Avant le processus d'électrodéposition, les substrats d'ITO sont systématiquement nettoyés par ultrason avec l'acétone (CH_3COCH_3) et l'éthanol (C_2H_5OH) durant 10 minutes. Après chaque passage dans un solvant, les substrats sont rincés avec l'eau distillée et finalement ils sont séchés à l'air libre. On utilise ces étapes pour enlever les différents contaminants recouvrant la surface du substrat (les graisses, les poussières, les empreintes,…). La morphologie de surface et la rugosité des films obtenus ont été examinées à l'aide d'une microscopie électronique à balayage MEB (JEOL NeoScope JCM 5000) et la microscopie à force atomique AFM (MFP-3D Oxford Instruments Asylum Research), respectivement. La structure et la composition de phase ont été identifiées par l'analyse de diffraction des rayons X (DRX) sur un diffractomètre Siemens D5000 en utilisant un rayonnement Cu Kα (λ = 1.5406 Å).

2.2 Préparation des couches minces de CuO

L'élaboration des couches minces CuO a été réalisée sur un substrat ITO par deux processus distincts: Electrodéposition des couches minces de Cu_2O et le traitement thermique par recuit de ces films obtenus à 500 °C pendant 1 h. Les films minces de Cu_2O ont été déposés électrochimiquement sur le substrat ITO dans une solution aqueuse contenant 0.05 M de sulfate de cuivre ($CuSO_4$, $5H_2O$) et 0.1 M de l'acide citrique ($C_6H_8O_7$) à 60°C. Le pH a été ajusté à 12 en ajoutant une quantité appropriée d'hydroxyde de sodium (NaOH) à la solution d'électrolytique.
La figure 1 montre les images photographiques des couches minces avant et après le traitement thermique. Les images photographiques montrent clairement une couleur jaune et la transparente des couches de Cu_2O sur le substrat. Nous avons observé aussi qu'il y a un changement notable de la couleur jaune vers le marron-noir après les traitements thermiques de ces couches à température de 500°C pendant 1h.

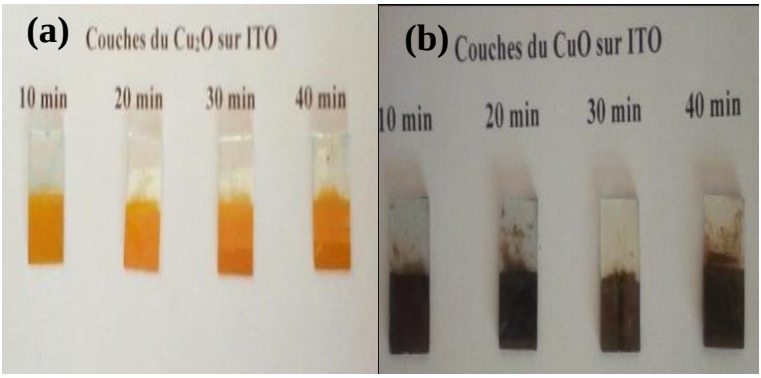

Figure 1. Images photographiques des couches minces de Cu_2O déposées sur une substrat ITO à différents temps avant le recuit thermique (a) et CuO après le recuit thermique (b).

3. Résultats set discussion

3.1 Courant transitoires

La figure 2 montre les courbes chronoampérométriques lors de la déposition de Cu_2O à un potentiel de - 0.5 V/ECS à différent temps de déposition (20, 30 et 40 min) avec un pH=12.

Nous observons que toutes les courbes chronoampérométriques présentent une forme typique d'un processus de nucléation limitée par la diffusion. Au début, une augmentation rapide de la densité de courant correspond la charge de la double couche et la formation des premiers germes de Cu_2O sur les sites actifs de la surface du substrat. Ensuite, le courant diminue sous l'effet de la croissance des germes jusqu'à ce que la densité de courant atteigne un maximum du courant i_{max} pour un temps t_{max}. Ensuite, la densité de courant augmente indiquant la réponse d'un système électrochimique sous contrôle diffusionel.

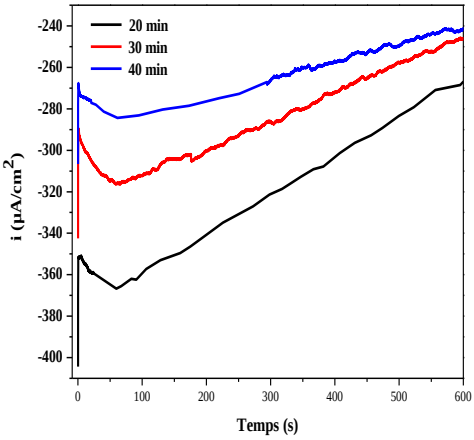

Figure 2. Courbes chronoampérométriques des couches minces de Cu_2O obtenues à différents temps de déposition.

3.2 Caractérisation structural

Afin de connaître les phases composant les différents échantillons, nous avons effectué des analyses par la diffraction des rayons X dans une gamme comprise entre 32° et 80°. La figure 3 montre les diffractogrammes des couches de Cu_2O obtenues a - 0.5 V/ECS à temps de déposition de 20 min avant et après le recuit à température 500 °C pendant 1h. Les pics marqués par des étoiles sont attribués à la phase tétragonale du substrat ITO. Avant le recuit, nous remarquons l'apparition de plusieurs pics correspondant à la phase cubique de Cu_2O polycristalline [14]. Ces pics ont été indexés selon la fiche JCPDS N° 00–005–0667, et ils correspondent aux plans (111), (200), (220) et (311), suivant de valeurs 2θ de 36.50°, 42.32°, 61.40° et 73.54°, respectivement. Aucun autre pic relatif au cuivre métallique (Cu) ou l'oxyde de cuivre (II) (CuO) n'a été observé confirmant ainsi la pureté de dépôt élaboré. Après le recuit (500 C°), la couche de Cu_2O se transforme en CuO. Ceci est indiqué par la disparition des pics de Cu_2O et l'apparition des nouveaux pics (-110), (002), (111), (-202), (201), (-113) et (220), suivant de valeurs 2θ de 32.70, 35.81, 38.96, 49.10, 58.48, 61.85 et 68.18, respectivement. Ces pics correspondant à la structure monoclinique de CuO (JCPDS 00-044-0706) [1, 13, 15]. Aucune autre phase telle que Cu_2O, Cu métallique et $Cu(OH)_2$ n'ont été observées ce qui signifie que la couche obtenue après le recuit a une pureté très élevée.

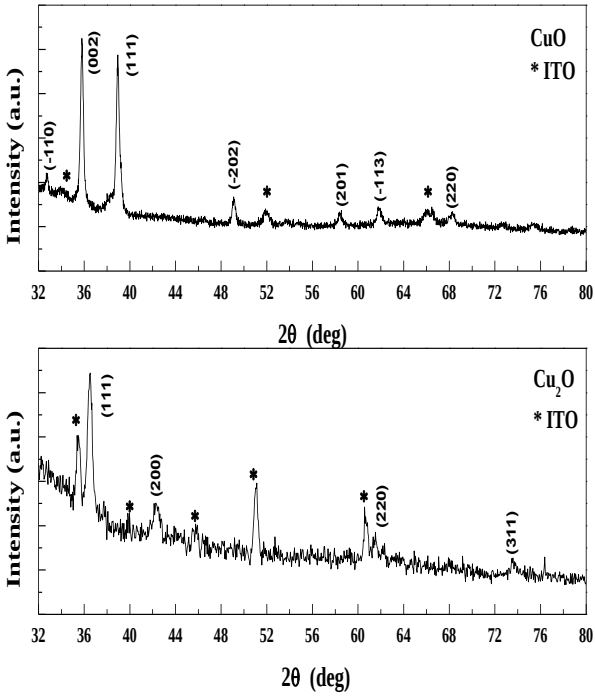

Figure 3. Spectres des rayons X pour les dépôts du Cu_2O électrodéposés sur ITO avant et après le recuit.

3.3 Caractérisation morphologique par AFM

En premier lieu, les films minces de Cu_2O élaborés à différents temps de déposition à température fixé de 60 °C sont subis une caractérisation morphologique par AFM. La figure 4 montre les images AFM 2D les films de Cu_2O/ITO déposés à différents temps de déposition avant le traitement thermique. Une distribution totale du dépôt sur la surface du substrat d'ITO a été observée sur la figure 4 avec une diminution de la taille des grains lorsque le temps de déposition augmente. On note également que la forme des grains est cubique avec une déformation de leur forme lorsque le temps déposition augmente.

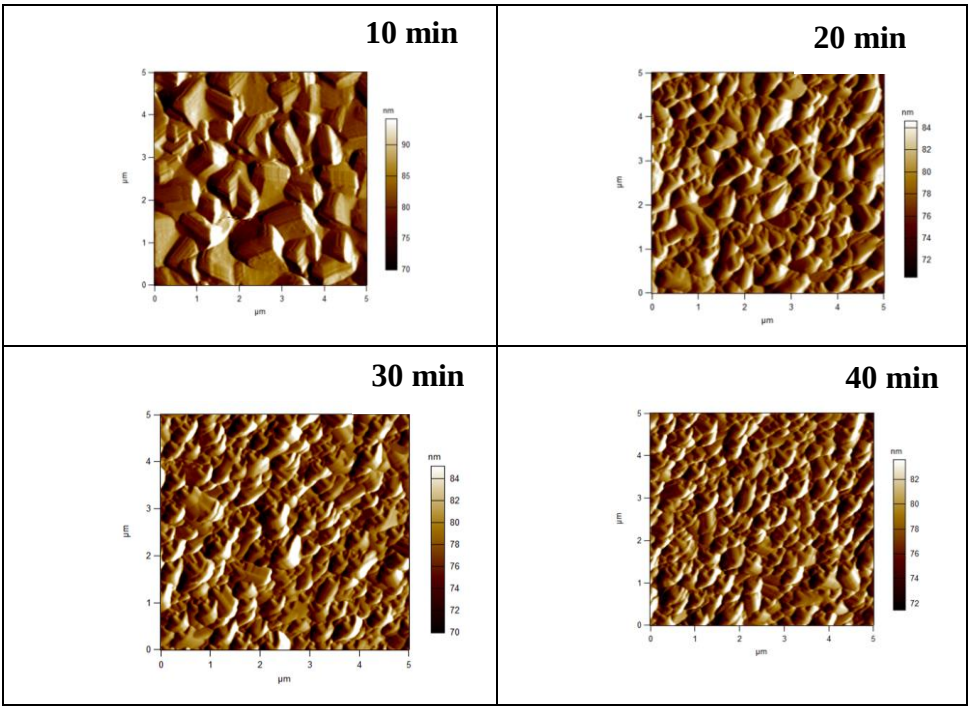

Figure 4. Images AFM 2D des couches minces de Cu_2O obtenus à différents temps avant le recuit.

Les valeurs de la rugosité de surface (RMS) obtenus à différents temps de déposition sont représentées dans la figure 5. Nous remarquons que la rugosité des couches minces de Cu_2O augmente avec le temps, puis elle est diminuée après 30 min. En second lieu, les couches de Cu_2O qui déjà synthétisés ont subi un traitement thermique à température de 500°C pendant 1h pour obtenir des films mince de CuO. La topographie et la rugosité de ces dépôts ont été étudiées aussi par AFM (Figure 6).

Nous remarquons tout d'abord une distribution totale et homogène des particules sur la surface du substrat quelle que soit la valeur de temps appliqué. La variation du temps de déposition n'a pas vraiment influencé la topographie des couches minces, car tous les échantillons présentent une forme granulaire. La taille de ces dernières diminue avec le temps tout en conservant sa topographie.

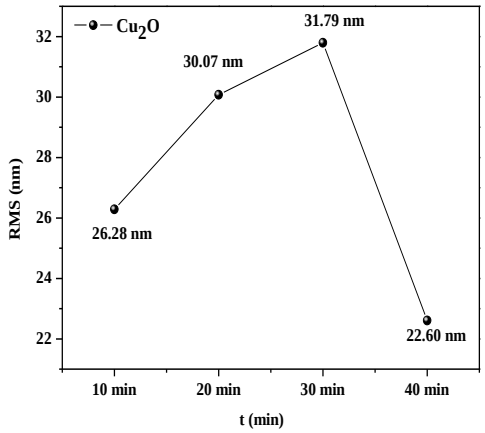

Figure 5. Evolution de la rugosité (RMS) des couches minces de Cu_2O en fonction du temps appliqués.

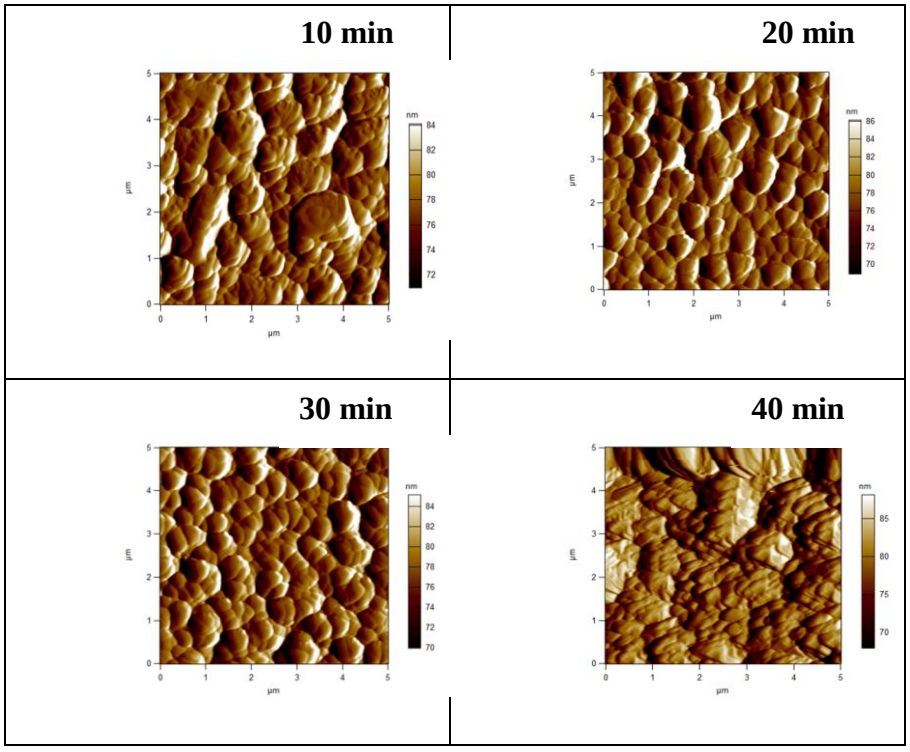

Figure 6. Images AFM en 2D des couches minces de CuO obtenus sur ITO à différents temps de déposition après le recuit.

Les valeurs de RMS obtenus à différents temps des dépôts CuO sont représentées dans la figure 7. Après le recuit, les valeurs de la rugosité moyenne passent de 38.26 à 76.22 nm lorsque le temps augmente 10 à 40 min.

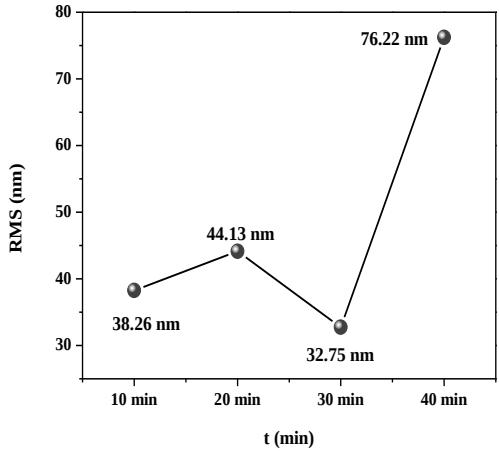

Figure 7. Evolution de la rugosité (RMS) des couches minces de CuO en fonction du temps appliqués.

3.4 Caractérisation morphologique par MEB

La morphologie de surface des couches minces de Cu_2O et de CuO a été étudiée par MEB dans l'échelle d'agrandissement de 1 μm (Figure 8). Les images MEB montré que la couche de Cu_2O ne recouvrent pas toute la surface de substrat avec une forme cubique [14-16]. Cependant, la couche de CuO est continu, homogène [13, 16, 17] recouvrant toute la surface de l'échantillon et caractérisé par des grains avec une forme nodulaire [6]. Ce résultat est en accord avec les résultats des travaux de Niveditha et al [17]. La taille des grains des couches minces CuO est plus petite que celle des couches Cu_2O.

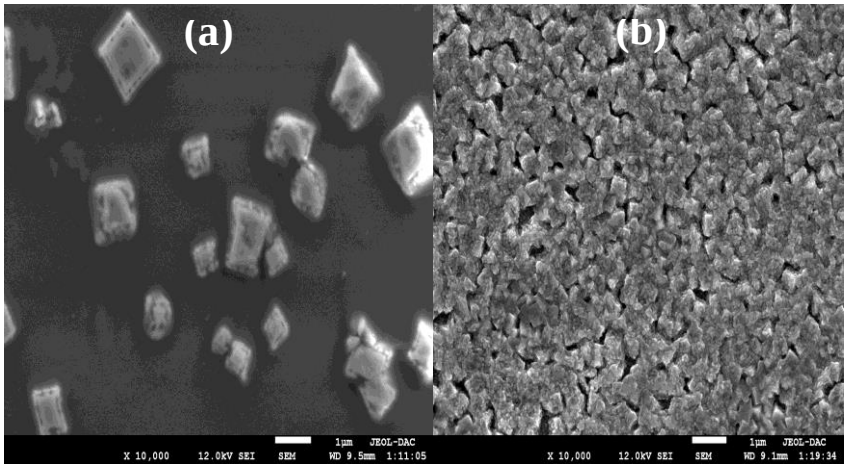

Figure 8. Image MEB de la couche mince élaborée à -0.5 V/ECS et 20 min sur ITO : a) Cu_2O et b) CuO.

3.4 Propriété Optique

L'étude de l'absorption des différentes couches de Cu_2O et CuO nous aide à estimer la valeur de l'énergie de gap optique (Eg) à partir de la relation de Tauc [18]. Pour chaque dépôt, en traçant $(\alpha h\upsilon)^2$ en fonction de l'énergie des photons $h\upsilon$, nous obtenons les tracés de Tauc qui sont représentées dans la figure 9. La valeur de Eg est déterminée à partir de l'extrapolation de la partie linéaire des tracés de Tauc en abscisse lorsque $\alpha = 0$.

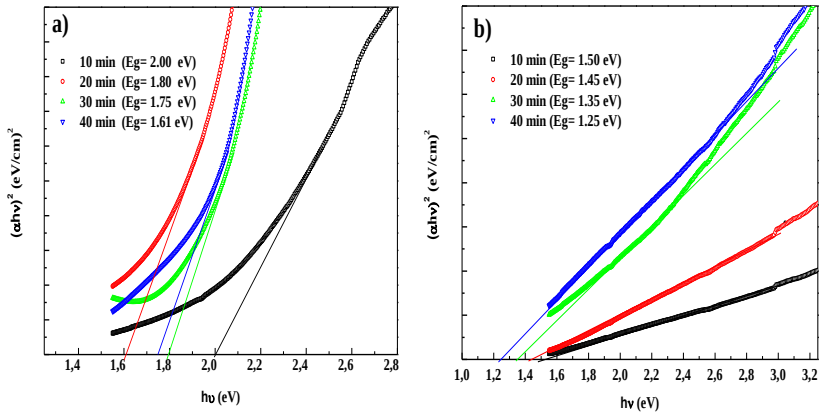

Figure 9. Tracés de Tauc des couches minces de (a) Cu2O et (b) CuO déposées à différents temps de déposition.

Les valeurs de la bande interdite des couches d'oxyde de cuivre se situent entre 1.60-2.00 eV et 1.25-1.50 eV pour les couches de Cu_2O et CuO, respectivement. Ces valeurs sont comparables à ceux trouvées dans la littérature [4-6]. D'après ces résultats, nous pouvons constater que la diminution de la valeur de gap optique avec l'augmentation du temps de dépôt est due à l'augmentation de l'épaisseur.

3.5 Test de photodégradation

L'oxyde de cuivre à des propriétés optiques et photoélectrochimiques très intéressantes qui pourrait permettre d'utiliser comme un photocatalyseur pour la dépollution de l'eau notamment dans les pays très ensoleillés. Le processus photocalytique implique l'activation d'un film de d'oxyde de cuivre (Cu_2O et CuO) par la lumière naturelle ou artificielle [17]. La figure 10 montre l'évolution des spectres d'absorption UV-Vis de méthyle orange (MO) en fonction du temps d'illumination en présence des couches minces Cu_2O et CuO à température ambiante sans agitation, la concentration de colorant a été fixer. Les spectres d'absorbance à différents temps d'illumination montrent que l'absorbance diminue légèrement avec l'augmentation du temps d'irradiation UV (λ = 465 nm), ce qui indique que la concentration de méthyle orange diminue avec l'augmentation du temps d'illumination et par conséquent de la dégradation de MO. On remarque aussi que le pic d'absorption à 463 nm diminue légèrement avec le temps d'irradiation UV en présence de Cu_2O (Figure 10a et b).
L'évolution des spectres d'absorption UV-Vis de MO en fonction du temps d'irradiation UV, en présence d'oxyde de cuivre CuO est représentée sur la figure 10c et d. D'après les deux figures on constate que les spectres d'absorbance diminuent de manière significative avec le temps d'irradiation UV, ce qui indique la dégradation et la diminution de la concentration d'OM avec le temps d'irradiation. La photodégradation du colorant se produit lorsque le rayonnement UV réagit avec la couche mince CuO en solution organique, ou des électrons et des trous sont générés. Les électrons font la transition vers la bande de conduction, laissant un trou dans la bande de valence. Les électrons et les trous agissent respectivement comme agent réducteur et oxydant. Les trous oxydent les molécules de H_2O, créant des espèces radicalaires oxydantes (radical réactif -OH) qui oxydent directement le polluant organique, tandis que les électrons réduisent l'oxygène adsorbé sur la surface du photocatalyseur [19].

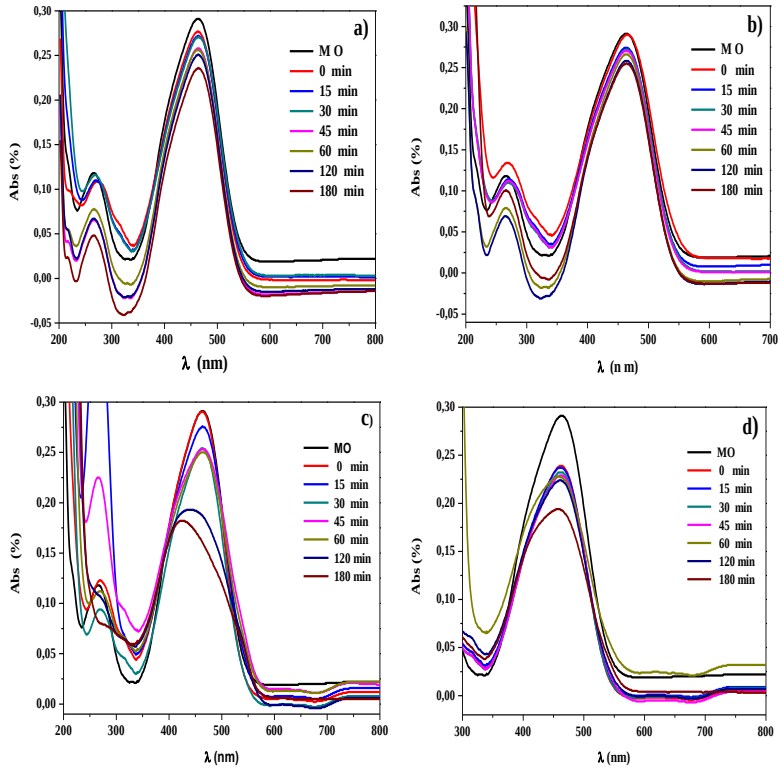

F**igure 10.** Evolution des spectres d'absorption UV-Visible de méthyle-orange en fonction du temps à 25°C de : Cu_2O: **a)** 20 min et **b)** 40 min ; de CuO : **c)** 20 min et **d)** 40 min sous irradiation UV (λ = 465 nm).

Le rapport C/C_0 en fonction de temps pour les deux échantillons (Cu_2O et CuO) est présenté sur la figure 11. On remarque que le taux de dégradation augmente de maniéré significatif en fonction de temps d'irradiation UV pour les deux échantillons. Ensuite, on observe une diminution du taux de dégradation de MO avec le temps de dépôt, qui augmente pour le filme Cu_2O de 13.4 % à 21.79 % pour 20 min et 40 min, respectivement. Cela indique que le Cu_2O déposé à 40 min possède une bonne activité photocatalytique à la dégradation du MO. Ces valeurs sont comparables avec celles obtenues dans d'autres travaux récents reportés pour la photodégradation de méthyle orange [20]. Par contre, On remarque une diminution de taux de dégradation de MO avec l'augmentation du temps de dépôt pour les films de CuO de 9.8 % à 4 .64 % pour 20 min et 40 min, respectivement. Il est également intéressant de noter que de nombreux paramètres expérimentaux jouent un rôle important dans le processus de catalyse; nous supposons que l'épaisseur

des particules, la morphologie et la dispersion des particules pourraient avoir un effet déterminant sur la catalyse [20].

Afin d'étudier la cinétique de la dégradation de méthyle-orange à l'aide des films élaborés d'oxyde de cuivre (Cu_2O/ITO et CuO/ITO), en trace $Ln\ C_0/C$ en fonction du temps d'irradiation selon le modèle cinétique de Langmuir-Hinshelwood [21]:

$$Ln\frac{C_0}{C} = k \qquad (1)$$

Où k est la constante de vitesse pseudo- première ordre, t le temps d'irradiation (s), C_0 la concentration initiale d'OM (M) et C la concentration de méthyle-orange au temps de l'irradiation (M).

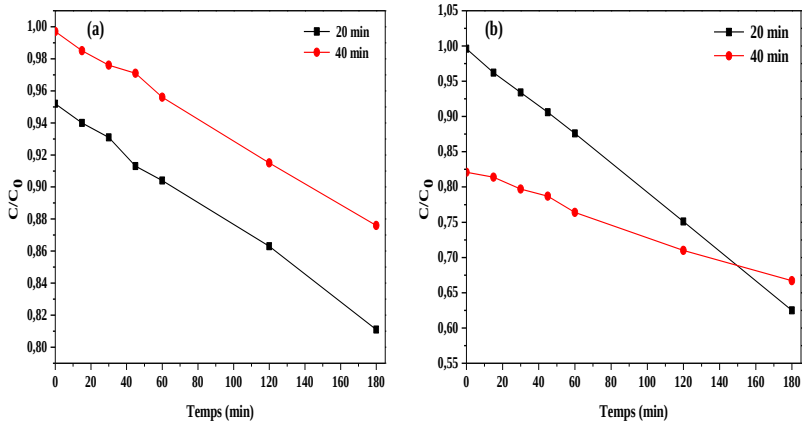

Figure 11. Dégradation de méthyle-orange en fonction du temps de Cu_2O (20, 40 min) à différent de temps de dépôt 20 min et 40 min sous irradiation UV (λ = 465 nm).

La constante de vitesse est calculée à partir de la courbe du logarithme du rapport de concentration en fonction du temps de réaction (Figure. 12). Les couche minces de l'oxyde de cuivre (Cu_2O et CuO) a des temps de déposition de 20 min et 40 min donne les meilleures vitesses de dégradation avec une constante de vitesse K de l'ordre 0,00087 min^{-1} pour Cu_2O et 0.0025 min^{-1} pour CuO avec une constante de corrélation R= 0.99555 et 0.99441 respectivement. Les valeurs de la constante de vitesse de dégradation photocatalytique obtenues sont plus importantes sur les couches de CuO que sur les coches Cu_2O. L'augmentation de la constante de vitesse est due à la conductivité élevée, donc un taux de génération d'électrons-trous élevé qui implique une meilleure dégradation [22].

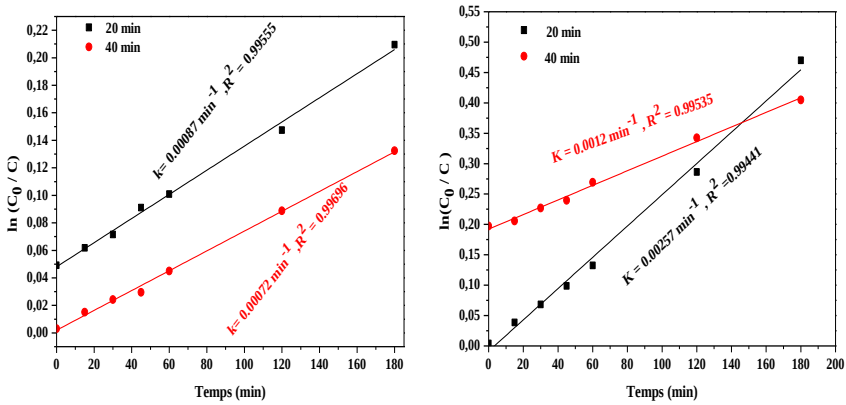

Figure 12. Cinétique du pseudo première ordre relatif a la dégradation d'OM par les couches mince de **a)** :Cu_2O et **b)** : CuO a défirent temps de dépôt 20 min et 40 min sous irradiation UV (λ = 465 nm).

4. Conclusion

Dans ce travail, nous avons élaborés des couches minces de Cu_2O sur des substrats d'ITO par l'électrodéposition à différents temps de déposition dans un bain sulfate. Les couches synthétisés ont subi un traitement thermique à température de 500 °C pendant 1h pour obtenir des films minces nommé CuO/ITO. La diffraction des rayons X a montré l'existence de deux structures cristallines de Cu_2O et CuO avant est après recuit, respectivement. La microscopie électronique à balayage a montré que les couches du Cu_2O sont hétérogènes avec une forme cubique, alors que les couches de CuO sont homogènes recouvrant toute la surface de l'échantillon avec une forme nodulaire. La microscopie à force atomique a montré une diminution de la taille des grains en fonction de l'augmentation du temps de déposition. La rugosité de surface (RMS) augmente aussi lorsque le temps de déposition augmente. Les valeurs du gap optique varient entre 1.60-2.00 eV pour Cu_2O et 1.25-1.50 eV pour CuO. Les tests photoctrocatalytiques montrent que le taux de dégradation de méthyle orange augmente avec le temps de déposition de Cu_2O. Par contre, pour les couches de CuO le taux de dégradation diminution avec l'augmentation du temps.

References

[1] H. Lee, X. Zhang, E. Kim, J. Park, Sensor. Mater. **31** (2019) 501-507.
[2] S. Dolai, R. Dey, S. Hussain, R. Bhar, A. K. Pal, Mater. Res. Bull. **109** (2019) 1-9.
[3] K. E. R. Brown, K.S Choi, Chem. Comm. **31** (2006) 3311-3313.
[4] P. Samarasekara, GESJ: Phys. **4** (2010).

[5] X. Zhang, G. Wang, X. Liu, J. Wu, M. Li, J. Gu, H. Liu, B. Fang, J. Phys. Chem. C **112** (2008) 16845-16849.
[6] Y. Chen, D. Yan, X. Jin, Y. Zeng, D. Zhang, Z. Liu, W. He, S. Wang, Z. Wang, Y. Liu, W. Zhang, Y. Huang, Appl. Surf. Sci. **491** (2019) 206-215.
[7] T. Ikuno, J. Zheng, A. Vjunov, M. Sanchez-Sanchez, M. A. Ortuño, D. R. Pahls, J. L. Fulton, D.M. Camaioni, Z. Li, D. Ray, B.L. Mehdi,N. D. Browning, O. K. Farha, J. T. Hupp, C. J. Cramer, L. Gagliardi, J. A. Lercher , J. Am. Chem. Soc. **139** (2017) 10294-10301.
[8] F. Teng, W. Yao, Y. Zheng, Y. Ma, Y. Teng, T. Xu, S. Liang, Y. Zhu, Sensors and Actuators B:Chemical. **134** (2008) 761-768.
[9] M. Lakhdari, F. Habelhames, Mater. Sci: Mater. Electron. **30** (2019) 6107-6115.
[10] H. Tong, S. Ouyang, Y. Bi, N. Umezawa, M. Oshikiri, J. Ye, Adv. Mater. **24** (2012) 229-251.
[11] R. Shi, J. Lin, Y. Wang, J. Xu, Y. Zhu, J. Phys. Chem. C. **114** (2010) 6472-6477.
[12] F.J. Zhang, S.F. Zhu, F. Z. Xie, J. Zhang, Z.D. Meng, Separa. Purifica. Techno. **113** (2013) 1-8.
[13] D. Chu, J. Mo, Q. Peng, Y. Zhang, Y. Wei, Z. Zhuang, Y. Li, Chem. Cat. Chem. **3** (2011) 371-377.
[14] T. Mahalingam, V. Dhanasekaran, G. Ravi, S. lee, j. P. Chu, H-J. Lim, J. Optoelectron. Adv. Mater. **12** (2010) 1327-1332.
[15] M. J. Siegfried, K. S. Choi, J. Electrochem. Soc. **154** (12) (2007) D674-D677.
[16] X. Zhang, J. Song, J. Jiao, X. Mei, Solid. State. Sci. **12** (2010) 1215-1219.
[17] C. V. Niveditha, M. J. Jabeen-Fatima, S. Sindhu, Nanosys: Phys. Chem. Math. **4** (2016) 747-751.
[18] Z. Zhou, Z. Zhu, F. Cui, J. Shao, H. S. Zhou, Microchim. Acta. **187** (2020) 2-8.
[19] M. A. Khan, H. Mahmood, M.S. Khan, T. Iqbal, P. Ahmad, M. Shafique, M. Naeem, J. Solid. State. Electrochem. **24** (2020) 1123-1132.
[20] L. Arfaouia, F. Janenea, S. Kouassc, S. Mignard, F. Touatia, H. Dhaouadia, Russ. J. Inorg. Chem. **64** (2019) 1687-1696.
[21] O. Gezici, M. Küçükosmanoglu, A. Ayar, Colloi. Inter. Sci. **304** (2006) 307-316.
[22] S. H. Kim, A. Umar, R. Kumar, A. A. Ibrahim, G. Kumar, Mater. Lett. **156** (2015) 121-124.

- **Aims and scope:** The Journal of Physical and Chemical Research is an English, French or arabic language peer–reviewed half yearly publication, open access journal, free of charges. The journal edited by: Laboratory of Materials Physics, Radiation and Nanostructures (LPMRN), Faculty of Sciences and Technology, Mohamed El Bachir El Ibrahimi University, Bordj-Bou-Arreridj, Algeria. It publishes regular research papers (articles) and short communications. The motivation for this journal is to encourage scientists to publish their experimental and theoretical results in the field of Physical, Chemical and the related subjects. Papers previously published elsewhere cannot be accepted for the journal. Submission must be done at the following email address: jpcr@univ-bba.dz . The acceptance for publication lies on the recommendations of at least two ad hoc referees, and of the editorial board, if necessary.

- **Topics:**
  - Astrophysics and astroparticles
  - Atomic and molecular physics
  - Biological physics
  - Chemical physics and physical chemistry
  - Computational science
  - Condensed matter
  - Fluids and fluid dynamics
  - Gravitation and cosmology
  - Instrumentation and measurement
  - Mathematical physics
  - Medical physics
  - Nuclear physics
  - Optics, quantum optics and lasers
  - Particle physics and field theory
  - Semiconductors
  - Soft matter, liquids and polymers
  - Statistical physics and nonlinear systems
  - Surfaces, interfaces and thin films
  - Thermodynamics
  - Statistical Mechanics and Thermodynamics
  - Molecular Spectroscopy
  - Quantum Chemistry
  - Computational Chemistry
  - Physical Chemistry of Life Sciences
  - Surface Chemistry
  - Catalysis
  - Physical Chemistry of Electrochemistry
  - Kinetics
  - Nanochemistry and Nanophysics
  - Liquid Crystals
  - Ionic Liquid
  - Photochemistry
  - Experimental article of Physical chemistry
  - Mathematical Chemistry